University of California

Ernest O. Lawrence Radiation Laboratory

A STUDY OF HYDROMAGNETIC WAVE PROPAGATION IN PLASMA

Berkeley, California

DISCLAIMER

ay 3

UCRL-10990
UC-20 Controlled
Thermonuclear Processes
TID-4500 (24th Ed.)

UNIVERSITY OF CALIFORNIA

Lawrence Radiation Laboratory
Berkeley, California

AEC Contract No. W-7405-eng-48

May 19, 1964

ERRATA

TO: All recipients of UCRL-10990 UC-20 Controlled Thermonuclear Processes

FROM: Technical Information Division

Subject: UCRL-10990, "A Study of Hydromagnetic Wave Propagation in Plasma," by George R. Spillman (Thesis), October 2, 1963.

Please make the following corrections on subject report:

Page 19, Eqs. (2.26a) and (2.26b). Change the initial minus sign (-) to minus or plus ($\mp$), i.e.,

$$b_r = \mp i k_v a_1 (k^2 - \ldots . \text{ etc.}$$

and

$$b_\theta = \mp \frac{i k^2}{\mu_0 \omega} \quad a_2 (k^2 \ldots . \text{ etc.}$$

Page 20. Change the last equation on the page to

$$- k_v C = D (k^2 - k_v^2)^{1/2}.$$

Page 21. Change the first equation to

$$\frac{b_z}{b_r} = - a (k^2 - k_v^2)^{1/2} \quad \frac{Z_0 [a(k^2 - k_v^2)^{1/2}]}{Z_1 [a(k^2 - k_v^2)^{1/2}]} .$$

Change Eq. (2.28) to

$$\frac{A_{n2}}{A_{n1}} = - \frac{\left[\frac{1}{U_{n1}} - i k_{cn} a\right]}{\left[\frac{1}{U_{n2}} - i k_{cn} a\right]}$$

Page 21. Change Eq. (2.29) to

$$\frac{A_{n2}}{A_{n1}} = -\left(\frac{\frac{1}{p_{n1}} - ia}{\frac{1}{p_{n2}} - ia}\right)$$

Change the equation below Eq. (2.29) to

$$\frac{A_{n2}}{A_{n1}} = -\left(\frac{\lambda_{n1} - 2\pi ia}{\lambda_{n2} - 2\pi ia}\right) .$$

In the next-to-last paragraph, delete the sentence

"Therefore one would expect excitation resonances at $\lambda_{ni} = 11.9$ cm."

Page 23. Substitute new Fig. 6.

Page 24. Substitute new Fig. 7.

Page 32. In the equation at the bottom of the page, the quantity after the summation sign should be

$$\frac{1}{q^3} e^{\chi q/kT} .$$

Page 66. Change the fourth line to read

"driving end drops sharply to 1.5 at 5 Mc/sec.)"

In lines 11 and 12, delete "as do the excitation resonance frequencies that occur at $\lambda_{ni} = 2\pi a$ (See Sec. II-D)."

Pages 75 and 76. Delete the entire paragraph that begins on page 75 and ends on page 76.

UCRL-10990 + errata
UC-20 Controlled
Thermonuclear Processes
TID-4500 (19th Ed.)

UNIVERSITY OF CALIFORNIA
Lawrence Radiation Laboratory
Berkeley, California

Contract No. W-7405-eng-48

A STUDY OF HYDROMAGNETIC WAVE PROPAGATION IN PLASMA

George R. Spillman

(Thesis)

October 2, 1963

Printed in USA. Price $2.25. Available from the
Office of Technical Services
U. S. Department of Commerce
Washington 25, D.C.

A STUDY OF HYDROMAGNETIC WAVE PROPAGATION IN PLASMA

Contents

A STUDY OF HYDROMAGNETIC WAVE PROPAGATION IN PLASMA

George R. Spillman

Lawrence Radiation Laboratory
University of California
Berkeley, California

October 2, 1963

ABSTRACT

An investigation of the excitation of torsional and compressional hydromagnetic waves, and of the dispersion relation of the torsional wave in a cylindrical deuterium plasma is reported. The theory of azimuthally symmetric waves in a cylinder is reviewed and an expression is derived for the relative excitation of the two wave types by a current between concentric electrodes. The wave type propagating in the cylinder at various frequencies is established by simultaneous measurements of the r and θ components of the wave magnetic field, and the dispersion relation of the torsional wave is measured in the frequency range 0.04 to 0.48 times ion-cyclotron frequency. (The upper frequency limit is due to domination of the compressional wave at higher frequencies.) The measured wave velocity agrees with theoretical calculations of the velocity based on the average of the spectroscopically measured ion density. Scatter in attenuation measurements is too large to give good agreement with the theoretical attenuation, however, the proper general trend is observed. Observations of a plasma surface wave are reported in Appendix B.

I. INTRODUCTION

Hydromagnetic waves were first described in 1942 by Hannes Alfvén,[1] who suggested that waves of this type might account for the existence of sun spots. In the simplest case, these waves may be regarded as transverse oscillation of magnetic field lines carrying with them a perfectly conducting inviscid fluid, and the wave has a velocity along the field lines, $V = B/\sqrt{\mu_0 \rho}$, where B is a static magnetic induction and ρ is the fluid density (in rationalized mks units). His work was followed by treatment of these waves by Walén,[2] Åström,[3] and Herlofson.[4] Until recently little had been done experimentally. The reasons for this are found in the considerations of Lundquist[5] who showed that, for laboratory-size experiments with practical magnetic fields, fluids of very high conductivity are required to obtain waves that are not strongly damped. Initially, experiments were performed in liquid sodium and mercury by Lundquist[5] and Lehnert.[6]

In recent years a number of experiments have been performed in plasmas. The wave attenuation is approximately inversely proportional to both the conductivity and the Alfvén speed; hence, although the conductivity of laboratory plasmas is usually quite low, the greatly increased Alfvén speed over that of liquid metals makes plasma an attractive medium for wave experiments.

Reports of the experimental excitation and observation of hydromagnetic waves were made almost simultaneously in 1959 by Allen et al. in hydrogen plasma[7] and by Jephcott in noble-gas plasmas.[8] More detailed studies were reported by Wilcox et al.[9] and DeSilva.[10] Nagao and Sato[11] have measured the dispersion of such waves in ionized air, and recently Jephcott and Stocker have measured the dispersion in noble-gas plasmas.[12]

All the experiments mentioned above were performed in either cylindrical or toroidal geometry on a mode of propagation that is a torsional wave at frequencies far below the ion-cyclotron frequency and exhibits a resonance at ion-cyclotron frequency. Another wave

mode is compressional at low frequencies and exhibits a resonance at electron-cyclotron frequency and a low-frequency cutoff in cylindrical geometry. The latter mode has been studied by Swanson and Gould,[13] Jephcott,[14] and Swanson.[15]

Stix has proposed that the ion-cyclotron resonance of the torsional mode be utilized in heating ions of a deuterium plasma to thermonuclear temperatures.[16] Experiments on such heating are being carried out by Hooke, et al.,[17,18] Nazarov et al.,[19] and Boley et al.[20] In addition to providing basic information on plasma physics, experimental studies of wave propagation in deuterium plasma have been considered desirable to support such ion-cyclotron heating experiments.

In this study propagation of waves in a highly ionized, cylindrical deuterium plasma with a uniform magnetic field is investigated experimentally. Wave theory is reviewed and excitation of waves by a discharge between coaxial electrodes is considered. The phase velocity and attenuation of the torsional (T) wave are measured in the frequency range 0.04 to 0.48 times ion-cyclotron frequency. The upper frequency is limited by the appearance and domination of the compressional (TLA) mode. The propagation of a surface wave has also been observed and is reported in Appendix B.

II. THEORY OF AZIMUTHALLY SYMMETRIC HYDROMAGNETIC WAVES IN CYLINDRICAL PLASMA

A. Basic Equations

Most of this theory follows closely that presented by DeSilva.[10] We assume a uniform plasma enclosed in a cylinder with a uniform axial magnetic field, and use mks rationalized units in all wave derivations.

The basic equations are Maxwell's equations and the equations of motion for the particles. We consider a gas composed of ions, electrons, and neutral particles. From the second moments of the Boltzmann equation for ions and electrons (see for example Spitzer, p. 94[21]) we have

$$n_e m_e \left(\frac{\partial \underset{\sim}{v}_e}{\partial t} + \underset{\sim}{v}_e \cdot \nabla \underset{\sim}{v}_e \right) = - n_e e \underset{\sim}{E} - n_e e \underset{\sim}{v}_e \times \underset{\sim}{B} - \nabla p_e + \underset{\sim}{P}^{ei} + \underset{\sim}{P}^{en} \qquad (2.1)$$

and

$$n_i m_i \left(\frac{\partial \underset{\sim}{v}_i}{\partial t} + \underset{\sim}{v}_i \cdot \nabla \underset{\sim}{v}_i \right) = n_i e \underset{\sim}{E} + n_i e \underset{\sim}{v}_i \times \underset{\sim}{B} - \nabla p_i + \underset{\sim}{P}^{ie} + \underset{\sim}{P}^{in}, \qquad (2.2)$$

and for neutrals

$$n_n m_n \left(\frac{\partial \underset{\sim}{v}_n}{\partial t} + \underset{\sim}{v}_n \cdot \nabla \underset{\sim}{v}_n \right) = \underset{\sim}{P}^{ne} + \underset{\sim}{P}^{ni} - \nabla p_n . \qquad (2.3)$$

Here n_j is the density of jth-type particles, $\underset{\sim}{v}_j$ is the average velocity of jth species, m_j is the mass of jth-type particle, e is the electron charge, $\underset{\sim}{E}$ is the electric field strength, $\underset{\sim}{B}$ is the magnetic induction, p_j is the partial pressure of the jth species, and $\underset{\sim}{P}^{ij}$ is the momentum transfer per unit time per unit volume from the jth to the ith species ($\underset{\sim}{P}^{ij} = - P^{ji}$). In Eqs. (2.1) through (2.3) we assume $\nabla p = 0$, and $n_i = n_e$ (charge neutrality). We further assume that in equilibrium $\underset{\sim}{v}$ and $\underset{\sim}{E}$ are zero; $\underset{\sim}{B}$ equals $\underset{\sim}{B}_0$, the static magnetic field; and that departures from equilibrium are small, so that in Eqs. (2.1) through (2.3) we may set $\underset{\sim}{v} \cdot \nabla \underset{\sim}{v} = 0$ and replace $\underset{\sim}{B}$ by $\underset{\sim}{B}_0$.

We assume charge exchange to be the dominant momentum-transfer effect between ions and neutrals, and since $|\underset{\sim}{P}^{en}|$ is of order $(m_e/m_i)^{1/2}|\underset{\sim}{P}^{in}|$, we drop $\underset{\sim}{P}^{en}$ and write Eq. (2.3) as

$$\underset{\sim}{P}^{ni} = mn_n \frac{\partial \underset{\sim}{v}_n}{\partial t} = m(\underset{\sim}{v}_i - \underset{\sim}{v}_n)\, n_n \omega_{ni} ,$$

where ω_{ni} is the collision frequency of a neutral particle with ions. Assuming harmonic time dependence $v_n \sim \exp(-i\omega t)$, we obtain

$$\underset{\sim}{v}_n = \frac{1}{1 - i\omega/\omega_{ni}}\, \underset{\sim}{v}_i$$

$$\underset{\sim}{P}^{ni} = -i\omega mn_n \frac{1}{1 - i\omega/\omega_{ni}}\, \underset{\sim}{v}_i . \tag{2.4}$$

We next define the resistivity tensor $\underset{\sim}{\eta}$ by

$$\underset{\sim}{\eta} \cdot \underset{\sim}{j} = \frac{\underset{\sim}{P}^{ei}}{ne} , \tag{2.5}$$

where

$$\underset{\sim}{j} \equiv en(\underset{\sim}{v}_i - \underset{\sim}{v}_e) \tag{2.6}$$

We now add Eqs. (2.1) and (2.2), getting

$$n \frac{\partial}{\partial t}(m_e \underset{\sim}{v}_e + m_i \underset{\sim}{v}_i) = \underset{\sim}{j} \times \underset{\sim}{B}_0 + \underset{\sim}{P}^{in} .$$

We substitute Eq. (2.4) and $\underset{\sim}{v}_e = \underset{\sim}{v}_i - \underset{\sim}{j}/en$ from Eq. (2.6) into the above equation, obtaining

$$nm_e \frac{\partial \underset{\sim}{v}_i}{\partial t} - \frac{m_e}{e}\frac{\partial \underset{\sim}{j}}{\partial t} + nm_i \frac{\partial \underset{\sim}{v}_i}{\partial t} = \underset{\sim}{j} \times \underset{\sim}{B}_0 + \frac{i\omega mn_n}{1 - i\omega/\omega_{ni}}\, \underset{\sim}{v}_i$$

The first term on the left is of order m_e/m_i compared with the third term, and for waves of angular frequency ω, the second term is of order ω/ω_{ce}, where ω_{ce} is the electron-cyclotron angular frequency. Our range of interest for ω is $\omega < \omega_{ce}/1500$, hence we drop the first two

terms on the left and obtain

$$- i\omega\rho_i \underset{\sim}{v}_i = \underset{\sim}{j} \times \underset{\sim}{B}_0 + \frac{i\omega\rho_n \underset{\sim}{v}_i}{1 - i\omega/\omega_{ni}} ,$$

where we have used $\rho_j = m_j n_j$ and $\partial/\partial t = - i\omega$. We may write the above equation alternately as

$$- i\omega \left(\rho_i + \frac{\rho_n}{1 - i\omega/\omega_{ni}} \right) \underset{\sim}{v}_i = \underset{\sim}{j} \times \underset{\sim}{B}_0$$

In order to maintain a mathematically similar form to the case of 100% ionization, we define a complex density by

$$\rho_1 = \rho_i + \frac{\rho_n}{1 - i\omega/\omega_{ni}} . \tag{2.7}$$

This complex density will enter into an Alfvén velocity term (see next section), making it complex, and therefore will signify damping due to ion-neutral collisions.

Then we have

$$- i\omega\rho_1 \underset{\sim}{v}_i = \underset{\sim}{j} \times \underset{\sim}{B}_0 . \tag{2.8}$$

So far we have deduced only one equation from Eqs. (2.1) and (2.2), so we substitute for $\underset{\sim}{v}_e$ from Eq. (2.6) into Eq. (2.1) and again drop terms of order ω/ω_{ce}. We obtain a generalized Ohm's law:[21]

$$\underset{\sim}{E} + \underset{\sim}{v}_i \times \underset{\sim}{B} = \underset{\sim}{\eta} \cdot \underset{\sim}{j} + \frac{1}{en} \underset{\sim}{j} \times \underset{\sim}{B}_0 . \tag{2.9}$$

To these we add Maxwell's curl equations in linearized form,

$$\nabla \times \underset{\sim}{b} = \mu_0 \underset{\sim}{j} \tag{2.10}$$

and

$$\nabla \times \underset{\sim}{E} = - \frac{\partial \underset{\sim}{b}}{\partial t} , \tag{2.11}$$

where $\underset{\sim}{b}$ is a perturbing wave magnetic induction imposed on the static induction $\underset{\sim}{B}_0$. The displacement current in Eq. (2.10) has been neglected, since it is of order of the square of the ratio of the Alfvén velocity to the velocity of light. Equations (2.8) through (2.11) constitute the basic set to be solved for wave motion.

B. The Dispersion Relation

With a fair amount of algebraic manipulation (for details see DeSilva[10]) and using $\partial/\partial t = -i\omega$, Eqs. (2.8) through (2.11) may be put in the form

$$\frac{\omega^2}{V^2}\,\underset{\sim}{b} + \frac{\partial^2}{\partial z^2}\,\underset{\sim}{b} + \nabla^2 b_z \hat{z} - \nabla \frac{\partial b_z}{\partial z} + \frac{i\omega}{\mu_0 V^2}\,\nabla \times (\underset{\sim}{\eta} \cdot \nabla \times \underset{\sim}{b})$$

$$+ i\Omega \nabla \times \frac{\partial}{\partial z}\,\underset{\sim}{b} = 0, \qquad (2.12)$$

where $V \equiv B_0/(\mu_0 \rho_1)^{1/2}$ is the complex Alfvén velocity, $\omega_{ci} \equiv eB_0/m_i$ is the ion-cyclotron angular frequency, $\hat{z} \equiv \underset{\sim}{B}_0/B_0$ is the axial unit vector, and $\Omega \equiv (\rho_1/nm_i)(\omega/\omega_{ci})$ is the complex dimensionless frequency.

The resistivity tensor is assumed to be of the form

$$\underset{\sim}{\eta} = \eta_{\parallel}\,\hat{z}\hat{z} + \eta_{\perp}(\underset{\sim}{I} - \hat{z}\hat{z}),$$

where $\underset{\sim}{I}$ is the unit tensor. All these quantities are assumed constant and independent of position.

We define a dimensionless resistivity

$$a_{\perp} \equiv \frac{\omega\eta_{\perp}}{\mu_0 V^2}, \qquad a_{\parallel} \equiv \frac{\omega\eta_{\parallel}}{\mu_0 V^2}$$

and assume a wave solution of the form

$$\underset{\sim}{b} = \underset{\sim}{b}_0 f(r) \exp[-i(\omega t - pz)]$$

such that $\partial/\partial t = -i\omega$, $\partial/\partial z = ip$, and $\partial/\partial\theta = 0$. Equation (2.12) yields the following component equations

$$(\hat{r}) \quad -ia_\perp\left(\frac{1}{r}\frac{\partial}{\partial r}r\frac{\partial b_r}{\partial r}\right) + \left(-p^2 + \frac{ia_\perp}{r^2} + ia_\perp p^2 + \frac{\omega^2}{V^2}\right)b_r + ip^2\Omega b_\theta - ip\frac{\partial b_z}{\partial r} = 0$$

$$(\hat{\theta}) \quad -ia_\parallel\left(\frac{1}{r}\frac{\partial}{\partial r}r\frac{\partial b_\theta}{\partial r}\right) + \left(-p^2 + \frac{ia_\parallel}{r^2} + ia_\perp p^2 + \frac{\omega^2}{V^2}\right)b_\theta - ip^2\Omega b_r + p\Omega\frac{\partial b_z}{\partial r} = 0$$

$$(\hat{z}) \quad (1 - ia_\perp)\left(\frac{1}{r}\frac{\partial}{\partial r}r\frac{\partial b_z}{\partial r}\right) + \left(\frac{\omega^2}{V^2} - p^2(1 - ia_\perp)\right)b_z - p\Omega\frac{\partial b_\theta}{\partial r} + \frac{1}{r}b_\theta = 0.$$

By differentiating the last equation with respect to r and using the definition of the Bessel operator

$$S \equiv \frac{1}{r}\frac{\partial}{\partial r}\left(r\frac{\partial}{\partial r}\right) - \frac{1}{r^2},$$

we may rewrite the above equations as:

$$(-ia_\perp S + F)\,b_r + ip^2\Omega b_\theta - ip\frac{\partial b_z}{\partial r} = 0 \qquad (2.13a)$$

$$(-ia_\parallel S + F)\,b_\theta - ip^2\Omega b_r + p\Omega\frac{\partial b_z}{\partial r} = 0 \qquad (2.13b)$$

$$[(1 - ia_\perp)S + F]\frac{\partial b_z}{\partial r} - p\Omega S b_\theta = 0, \qquad (2.13c)$$

where $F \equiv (\omega^2/V^2) - (1 - ia_\perp)p^2$. The necessary condition $\nabla\cdot b = 0$ shows (a) and (c) to contain the same information. From the Eqs. (2.13) we may obtain the fourth-degree operator equation

$$(S + {}_1k_c^2)(S + {}_2k_c^2)(b_r\hat{r} + b_\theta\hat{\theta} - \frac{\partial b_z}{\partial r}\hat{z}) = 0 \qquad (2.14)$$

where for the algebraically simpler special case of $a_{\|} = a_{\perp} = a$, k_c and p are related through the dispersion equation

$$\Omega^2 p^2 (k_c^2 + p^2) - \left[\frac{\omega^2}{V^2} - (1 - ia)p^2 + iak_c^2\right] \times \left[\frac{\omega^2}{V^2} - (1 - ia)p^2 + iak_c^2 - k_c^2\right] = 0.$$

We rewrite this equation in two ways:

$$k_c^2 = \left\{ -\left[\Omega^2 p^2 + (1-2ia)\left\{\frac{\omega^2}{V^2} - (1-ia)p^2\right\}\right] \pm \left[\left(\Omega^2 p^2 + (1-2ia)\left\{\frac{\omega^2}{V^2} - (1-ia)p^2\right\}\right)^2 - 4ia(1-ia)\left(\Omega^2 p^4 - \left\{\frac{\omega^2}{V^2} - (1-ia)p^2\right\}\right)\right]^{1/2}\right\}\left[2ia(1-ia)\right]^{-1} \quad (2.15a)$$

and

$$p^2 = \frac{k_c^2}{2(1-ia)^2 - 2\Omega^2}\left\{ -(1-\Omega^2) + 2\beta^2(1-ia) + 2a^2 + 3ia \mp \left[(1-\Omega^2)^2 + 4\Omega^2\beta^4 - a^2 + ia\left(2(\Omega^2 - 1) + 4\Omega^2\beta^2\right)\right]^{1/2}\right\}, \quad (2.15b)$$

where we have defined $\beta^2 \equiv \omega^2/(V^2 k_c^2)$. Therefore our equation is double-valued in both p and k_c, and the general solution of Eq. (2.14) for a specified p is

$$b_\theta = C_1 J_1({}_1k_c r) + C_2 J_1({}_2k_c r), \quad (2.16)$$

with a similar equation for b_r. (We have excluded Neumann functions to avoid infinite solutions at the center of the tube.)

We shall require purely axially propagating wave solutions (i.e. no variations of the radial profile in time), which will place restrictions on k_c (see Appendix A). These restrictions will imply geometry-independent dispersion relations unless we set one of the C equal to zero. Disregarding geometry independence as unphysical, we set $C_2 = 0$, and obtain

$$b_\theta = C_1 J_1(k_c r), \quad (2.17)$$

where k_c is determined by boundary conditions. The existence of only one k_c^2 for each p^2 was also shown by DeSilva[10] for the particular boundary condition of a thin insulating layer between plasma and conducting cylinder, which is applicable for this experiment.

We now rewrite Eq. (2.15b) with subscripts

$$p_{1\atop 2}^2 = \frac{k_c^2}{2(1-i\alpha)^2 - 2\Omega^2}\left\{-(1-\Omega^2) + 2\beta^2(1-i\alpha) + 2\alpha^2 + 3i\alpha \right.$$
$$\left. \mp \left\{(1-\Omega^2)^2 + 4\Omega^2\beta^4 - \alpha^2 + i\alpha\left[2(\Omega^2-1) + 4\Omega^2\beta^2\right]\right\}^{1/2}\right\} \qquad (2.18)$$

which are the dispersion relations for two hydromagnetic modes. For the low-frequency case ($\Omega \to 0$) and for $\alpha << 1$, we have

$$p_2^2 = \frac{1}{1-i\alpha}\left(\frac{\omega^2}{V^2} + i\alpha k_c^2\right)$$

$$p_1^2 = \frac{1}{1-i\alpha}\,\frac{\omega^2}{V^2} - k_c^2,$$

from which we see that the subscript 1-type wave does not propagate for $\omega < k_c V$. This has been referred to by various authors as the TE mode, TLA mode, compressional mode, or fast wave. The other mode (subscript 2) has been referred to as the T mode, principal mode, or torsional mode. We will show the meaning of the designations torsional and compressional in the next section.

For $\alpha = 0$ and $\Omega \to 1$ the dispersion relations become

$$p_1^2 = \frac{\omega^2}{V^2}\left[\frac{1}{1+\Omega} - \frac{1}{2\beta^2} - \frac{1-\Omega^2}{8\beta^4\Omega}\right] \quad \text{(TLA wave)}$$

and

$$p_2^2 = \frac{\omega^2}{V^2}\left[\frac{1}{1-\Omega} - \frac{1}{2\beta^2} + \frac{1-\Omega^2}{8\beta^4\Omega}\right] \quad \text{(T wave).}$$

Because of the $(1-\Omega)^{-1}$ term, p_2^2 becomes very large near $\Omega = 1$ (the ion-cyclotron frequency). Inclusion of a small resistivity yields

$$\text{Im } p \approx \frac{\omega}{2V}\,\frac{\alpha}{(1-\Omega)^{3/2}};$$

hence damping of the T wave becomes very high near the ion-cyclotron frequency.

The distance along the axis in which the wave damps to $1/e$ ($L = 1/\mathrm{Im}\ p$) and the phase velocity ($v = \omega/\mathrm{Re}\ p$) are calculated from Eq. (2.18) and are plotted as a function of frequency in Figs. 1 and 2. Choice of the k_c values is discussed in the next section.

C. Wave Fields

Experimentally the appropriate boundary condition has been found to be $b_\theta(r_0) = 0$, where r_0 is a radius slightly smaller than the cylinder radius. This is probably due to the presence of a poorly conducting layer of gas at the tube wall (see DeSilva's section on radial distributions[10] and Appendix B of this report). The k_c is then determined by

$$J_1(k_c r_0) = 0,$$

which yields an infinite set of discrete k_c. A general solution of Eq. (2.14) must utilize all possible values of k_c and each of the two values of p for each k_c. For the wave magnetic fields, we write the general solutions as

$$b_\theta = \sum_n \left(C_{n1} e^{ip_{n1}z} + C_{n2} e^{ip_{n2}z} \right) J_1(k_{cn} r), \tag{2.19}$$

$$b_r = \sum_n \left(A_{n1} e^{ip_{n1}z} + A_{n2} e^{ip_{n2}z} \right) J_1(k_{cn} r), \tag{2.20}$$

and

$$b_z = \sum_n \left(\frac{ik_{cn}}{p_{n1}} A_{n1} e^{ip_{n1}z} + \frac{ik_{cn}}{p_{n2}} A_{n2} e^{ip_{n2}z} \right) J_0(k_{cn} r). \tag{2.21}$$

Equation (2.21) follows from Eq. (2.20) and $\partial/\partial\theta = \nabla \cdot b = 0$.

Complex amplitudes A_n and C_n must be determined by boundary conditions at $z = 0$ (input conditions); however, the A_n and C_n are not independent. We define $U \equiv p/k_c$, and from any of the Eqs. (2.13) we may obtain for either wave type

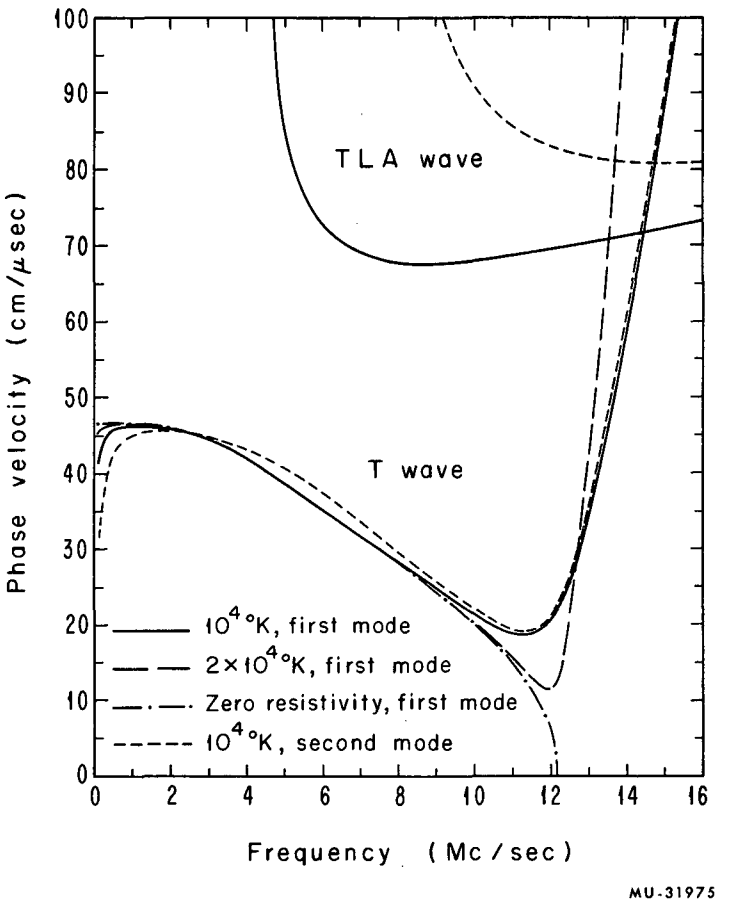

Fig. 1. Theoretical phase velocity versus frequency for the two types of waves as calculated from Eq. (2.18). Parameters for the calculation are a uniform magnetic field of 16 kG, a deuteron density of $2.85\times10^{15}/cm^3$ corresponding to the radially averaged spectroscopic measurement, no neutral particles, and a plasma radius of 7 cm. For the T wave, curves are presented for temperatures of 10^4°K, 2×10^4°K, and zero resistivity for the first radial mode, and for the second radial mode at 10^4 °K. For the TLA wave, temperature effects are too small to show in the figure.

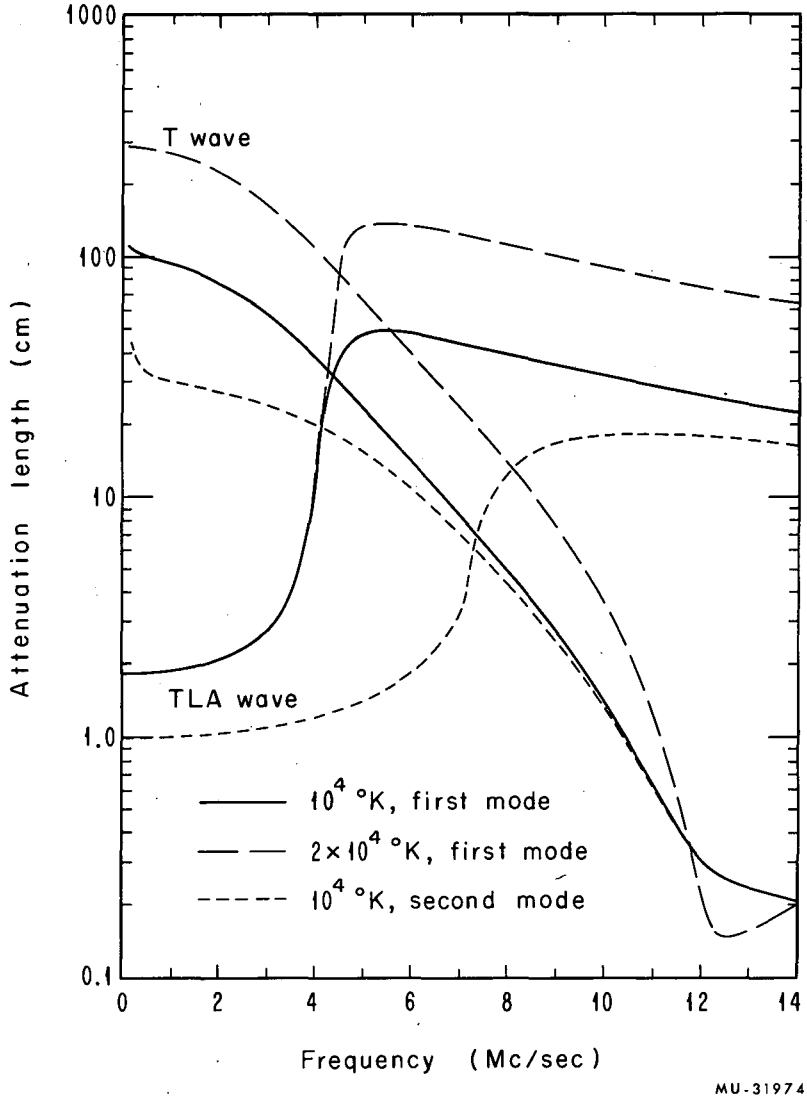

Fig. 2. Theoretical attenuation length versus frequency for the two wave types according to Eq. (2.18). Parameters are the same as for Fig. 1.

$$\frac{A_n}{C_n} = \frac{-iU_n^2\Omega}{\beta_n^2 - (1-i\alpha)(1+U_n^2)} . \qquad (2.22)$$

For a low frequency and $\alpha = 0$, by utilizing Eq. (2.18), we have

$$C_{n1} = i\Omega\beta_n^2 A_{n1} \qquad \text{(TLA, compressional)}$$

and

$$A_{n2} = i\beta_n^2 \Omega C_{n2} \qquad \text{(T, torsional).}$$

The designation as torsional or compressional wave becomes clear when one observes from the above Equations and Eq. (2.21) that for a low frequency the T wave is essentially a purely b_θ wave representing a torsion impressed upon the axial magnetic-field lines. The TLA wave, on the other hand, has very small b_θ at low frequencies, and is predominantly b_r and b_z, hence represents a compression of the axial magnetic field lines. At higher frequencies the three components become comparable for both wave types and the designation as torsional or compressional is no longer strictly correct.

The equations also show that in the T wave b_θ reaches a maximum one-quarter cycle before b_r. This means that the magnetic vector of the wave (and also the electric vector) rotates about the cylinder axis in the same sense as the ions (see Fig. 3). (This is the left-handed polarization as defined by Allis et al.[22]) The b vector for the TLA wave rotates in the same sense as the electrons. Since an electric field is also associated with the wave, at ion-cyclotron frequency an ion having an axial velocity that is negligible compared to the wave velocity may be constantly driven by the electric field of the T wave, thus providing a mechanism for absorption of wave energy by ions.

The other wave quantities may be derived from Eqs. (2.19) through (2.22), and (2.8) through (2.11). In the expressions given below,

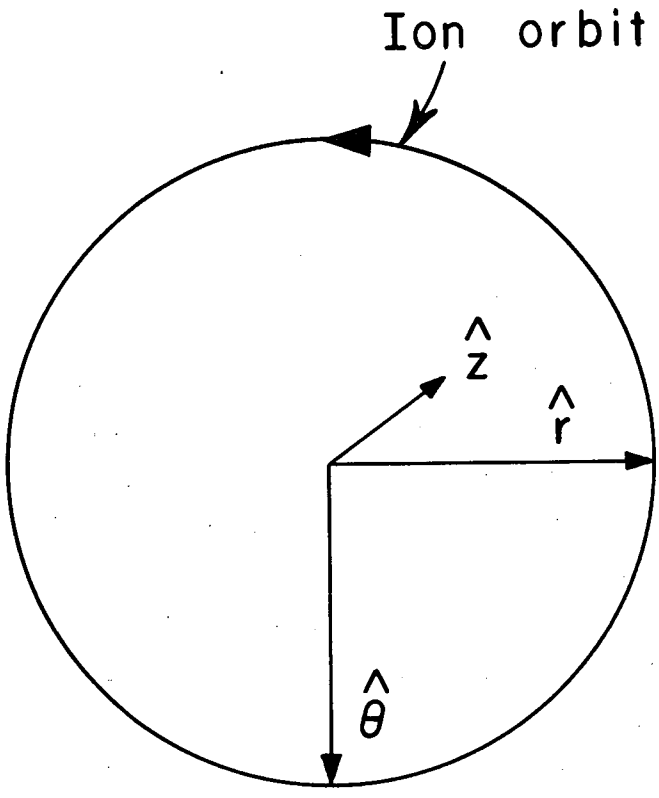

MU-31971

Fig. 3. Rotation of the wave's magnetic vector around the static magnetic field lines. The magnetic field is considered to be into the paper (z-direction) such that a deuteron will have a counterclockwise rotation. $\hat{r}, \hat{\theta}, \hat{z}$ form a right-handed system. Any vector having a θ-component maximum followed one-quarter cycle later by an r-component maximum rotates counterclockwise also.

which are valid for either wave type, the nth Bessel mode is assumed:

$$j_r = -i\frac{p_n}{\mu_0} C_n J_1(k_{cn}r),$$

$$j_\theta = \frac{i}{\mu_0 p_n}\left(p_n^2 + k_{cn}^2\right) A_n J_1(k_{cn}r),$$

$$j_z = \frac{k_{cn}}{\mu_0} C_n J_0(k_{cn}r),$$

$$v_{ir} = -\frac{V^2}{\omega B_0 p_n}\left(p_n^2 + k_{cn}^2\right) A_n J_1(k_{cn}r),$$

$$v_{i\theta} = -\frac{p_n V^2}{\omega B_0} C_n J_1(k_{cn}r),$$

$$v_{iz} = 0,$$

$$E_r = \frac{V^2}{\omega p_n}\left[(1 - i\alpha) p_n^2 C_n + i\Omega\left(p_n^2 + k_{cn}^2\right) A_n\right] J_1(k_{cn}r),$$

$$E_\theta = -\frac{\omega}{p} A_n J_1(k_{cn}r),$$

and

$$E_z = \frac{k_{cn} V^2}{\omega} \alpha C_n J_0(k_{cn}r).$$

D. Analysis of the Wave Drive into Radial Modes and Wave Types

The wave is excited by a discharge between coaxial electrodes (Fig. 4). We take as a first boundary condition $j_z = 0$ at $z = 0$ for radii larger than that of the center electrode. Then we have

$$(\nabla \times \underset{\sim}{b})_z = \frac{1}{r}\frac{\partial}{\partial r}(r b_\theta) = 0$$

which implies

$$b_\theta \sim \frac{1}{r}.$$

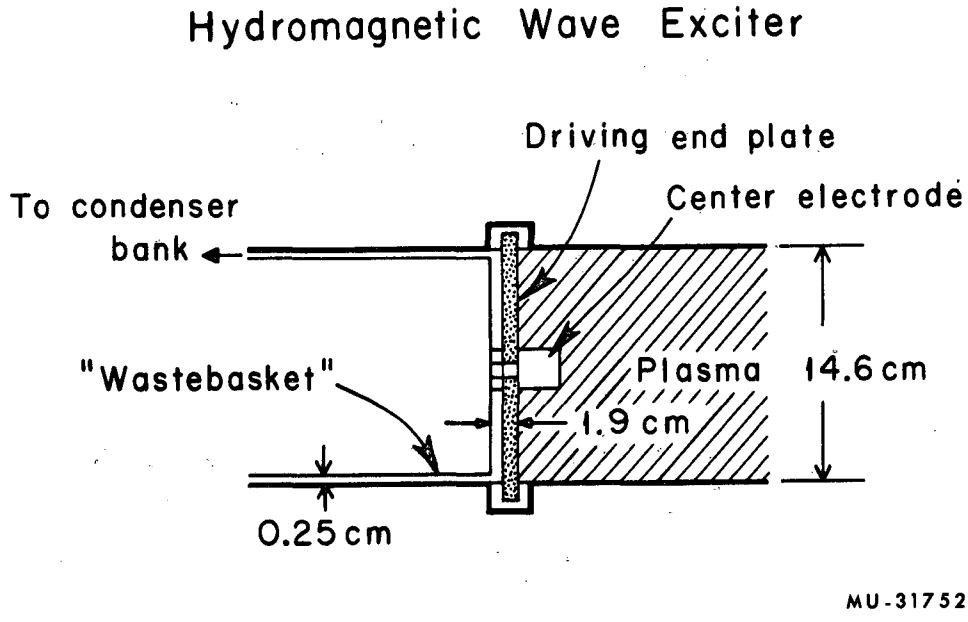

Fig. 4. Hydromagnetic wave generator. The "wastebasket" is the center conductor of a transmission line from the condenser bank which excites the wave to the center electrode. The distance between the wastebasket and outer conductor is considered infinitesimal and the wave solution in the cavity region between wastebasket and plasma is matched to the plasma wave solution to calculate partition between wave types. The cavity thickness a is taken as the distance between the wastebasket and the plasma (1.9 cm).

Matching vacuum fields immediately outside the plasma requires

$$b_\theta = \frac{\mu_0 I}{2\pi r}, \tag{2.24}$$

where I is the current through the electrode. (We assume azimuthal symmetry.) We now need to analyze b_θ into Bessel functions of order 1 having zeros at the cylinder wall. Since Eq. (2.24) does not have a zero, we assume the geometry to be modified to that of Fig. 5 and assume b_θ to be given by

$$b_\theta(r, 0) = \begin{cases} 0; \; r < r_e, \; r > r_0 \\ \mu_0 I / 2\pi r; \; r_e < r < r_0 . \end{cases}$$

This function may be analyzed into Bessel functions. We go to the limit $r_0 \to r_w$ and obtain for the Bessel coefficients

$$C_n = -\frac{\mu_0 I}{\pi r_w^2} \frac{J_0(k_{cn} r_w) - J_0(k_{cn} r_e)}{k_{cn} J_0^2(k_{cn} r_w)} \tag{2.25}$$

This expression is correct for either wave type or for any mixture of the two wave types.

The ratio of wave energy in any Bessel mode to the total wave energy is given by

$$\frac{W_n}{W_T} = \frac{2}{r_w \ell n(r_w / r_e)} \left[\frac{J_0(k_{cn} r_w) - J_0(k_{cn} r_e)}{k_{cn} J_0(k_{cn} r_w)} \right]^2.$$

Some numerical results are presented in Table I.

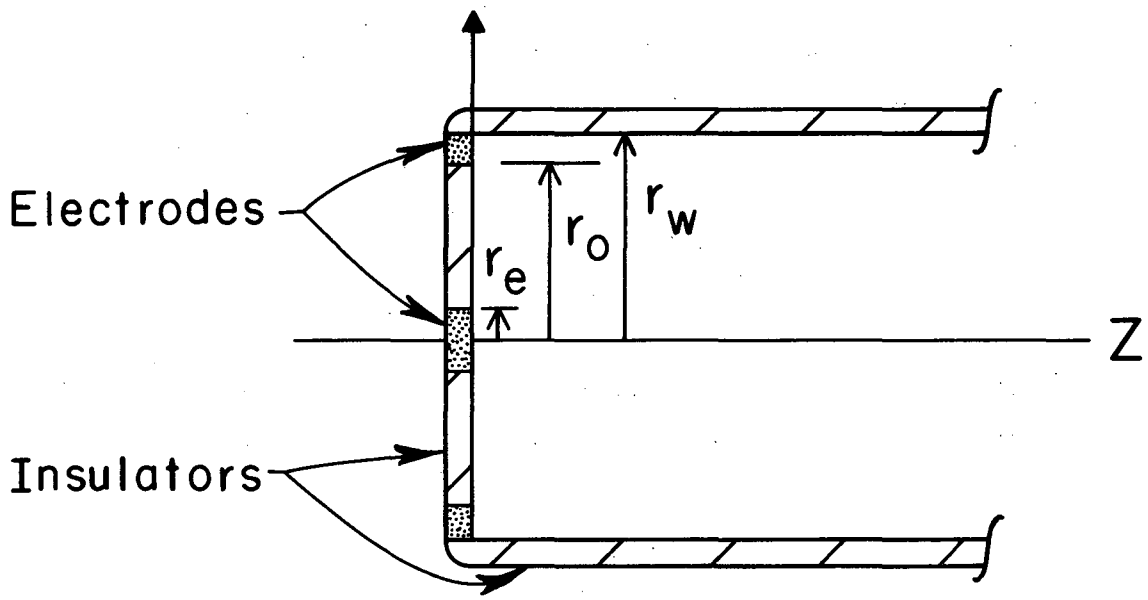

Fig. 5. Electrode arrangement assumed for modal analysis.

Table I. Results of analysis into radial modes

Mode number n	Total wave energy (%)	Peak value* of b_θ
1	79	1
2	7	0.39
3	0.7	0.16
4	4.3	0.43
5	2.5	0.37

*Normalized to lowest Bessel mode.

To analyze the initial disturbance into wave types, we match plasma wave solutions to the vacuum wave solution in the region between plasma and the "wastebasket" electrode lead (see Fig. 4). We assume the region between the "wastebasket" and the outer conductor to be too small to affect the solution. (This distance is about 0.25 cm, compared to an inside diameter of 14.6 cm for the outer conductor and a distance between the wastebasket and plasma of 1.9 cm). For the cavity region we can write (see for example Stratton[23])

$$b_r = - ik_v a_1 (k^2 - k_v^2)^{1/2} Z_1[(k^2 - k_v^2)^{1/2} r]\, e^{\pm ik_v z} \qquad (2.26a)$$

$$b_\theta = -\frac{ik^2}{\mu_0 \omega}\, a_2 (k^2 - k_v^2)^{1/2} Z_1 [(k^2 - k_v^2)^{1/2} r]\, e^{\pm ik_v z} \qquad (2.26b)$$

and

$$b_z = (k^2 - k_v^2) a_1 Z_0 [(k^2 - k_v^2)^{1/2} r]\, e^{\pm ik_v z}, \qquad (2.26c)$$

where we have again used $\partial/\partial\theta = 0$, Z_j is a linear combination of Bessel and Neuman functions of order j, and a_1 and a_2 are arbitrary constants. We temporarily take $z = 0$ at the wastebasket surface. We use Maxwell's curl equations in the form

$$\underset{\sim}{E} = \frac{1}{\sigma - i\omega\epsilon} \nabla \times \underset{\sim}{H}; \qquad \underset{\sim}{H} = \frac{1}{i\omega\mu} \nabla \times \underset{\sim}{E}.$$

and require $E_\theta(r, 0) = 0,$

which implies $\dfrac{\partial E_\theta(r, 0)}{\partial r} = 0.$

From the curl-E equation, we obtain $H_z(r, 0) = 0$, which implies

$$\frac{\partial H_z(r, 0)}{\partial r} = 0.$$

From the curl-H equation, we get

$$\frac{\partial H_r(r, 0)}{\partial z} = \frac{\partial H_z(r, 0)}{\partial r}.$$

We then take for the boundary conditions at the wastebasket

$$b_z = 0 \tag{2.27a}$$

$$\frac{\partial b_r}{\partial z} = 0. \tag{2.27b}$$

In obtaining these boundary conditions, we have used only the single condition $E_\theta(r, 0) = 0.$

The equations for b_r and b_z are then of the form

$$b_r = DZ_1[(k^2 - k_v^2)^{1/2} r] \cos k_v z e^{-i\omega t}$$

and

$$b_z = CZ_0[(k^2 - k_v^2)^{1/2} r] \sin k_v z e^{-i\omega t}$$

and from $\nabla \cdot b = 0$ [or Eq. (2.26)] it follows that

$$\frac{C \sin k_v z}{D \cos k_v z} = \frac{i(k^2 - k_v^2)^{1/2}}{k_v} \frac{\sin k_v z}{\cos k_v z}$$

For this experiment k_v was $\leq 2.5 \times 10^{-3}$ cm^{-1} and $z < 2$ cm; hence $k_v z < 5 \times 10^{-3} << 1$. For a cavity thickness a, we have a plasma boundary condition

$$\frac{b_z}{b_r} = \frac{Z_0[(k^2 - k_v^2)^{1/2} r]}{Z_1[(k^2 - k_v^2)^{1/2} r]} \; i(k^2 - k_v^2)^{1/2} a.$$

Since we have already assumed that Neumann functions do not exist in the plasma, we drop them from the above expression and let $k_c = (k^2 - k_v^2)^{1/2}$.

Then from Eqs. (2.20) and (2.21) we have

$$\frac{A_{n2}}{A_{n1}} = - \frac{\frac{1}{U_{n1}} - k_{cn} a}{\frac{1}{U_{n2}} - k_{cn} a} \tag{2.28}$$

or

$$\frac{A_{n2}}{A_{n1}} = - \frac{\frac{1}{p_{n1}} - a}{\frac{1}{p_{n2}} - a} \; . \tag{2.29}$$

For Im p << Re p in regions other than where $|1/p| \approx a$, this may also be written as

$$\frac{A_{n2}}{A_{n1}} = - \frac{\lambda_{n1} - 2\pi a}{\lambda_{n2} - 2\pi a} \; ,$$

where the λ's are the appropriate hydromagnetic wavelengths. For this experiment, if we assume the plasma boundary is the quartz driving end plate, a is 1.9 cm. Therefore one would expect excitation resonances at $\lambda_{ni} = 11.9$ cm.

Looking briefly at other conditions, we see that for large values of a such that

$$\left|\frac{1}{p_{n1}}\right|, \; \left|\frac{1}{p_{n2}}\right| << a$$

and for the maximum frequency of this experiment (14.5 Mc/sec), and the additional condition $a << 400$ cm (i.e., $k_v a << 1$) we have

$$\frac{A_{n2}}{A_{n1}} \to -1.$$

For the opposite case of $a \to 0$, we can write

$$\frac{A_{n2}}{A_{n1}} \to -\frac{p_{n2}}{p_{n1}} .$$

For the region Re $p >>$ Im p, this may be written

$$\frac{A_{n2}}{A_{n1}} \to -\frac{\lambda_{n1}}{\lambda_{n2}} .$$

Calculated ratios of the field component in the T wave to the field component in the TLA wave at the exciter are shown in Figs. 6 and 7.

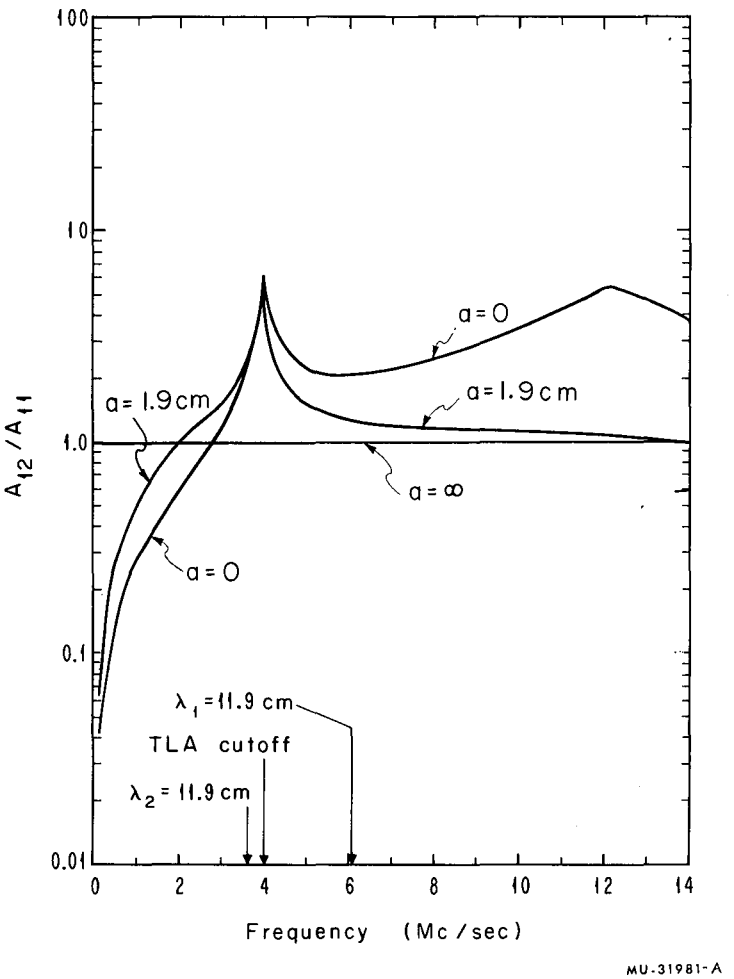

Fig. 6. Ratio of b_r excited into a torsional (T) wave to b_r excited into a compressional (TLA) wave for the lowest Bessel mode versus frequency according to Eq. (2.29) (A_{12}/A_{11} at driving-end plate). Parameters assumed are a deuteron density of $2.85\times10^{15}/cm^3$, no neutral particles, an electron temperature of 1.25×10^4 °K, a 16-kG static magnetic field and a plasma radius of 7 cm. Equation (2.20) defines A_{11} and A_{12}. Curves are shown for three values of a, the distance of the conducting plane from the plasma (see Fig. 5). The TLA cutoff frequency calculated for the experimental conditions is indicated.

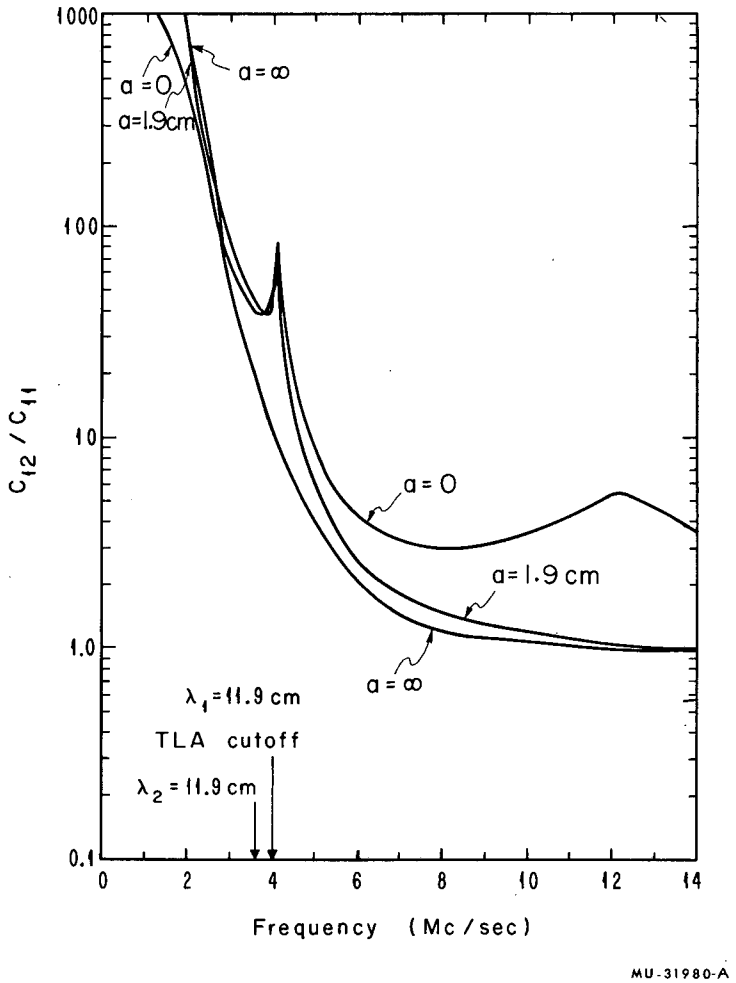

Fig. 7. Ratio of b_θ excited into torsional (T) wave to b_θ excited into compressional (TLA) wave versus frequency for the lowest Bessel mode and the same parameters as for Fig. 6 (C_{12}/C_{11} at driving-end plate). C_{11} and C_{12} are defined by Eq. (2.19).

III. EXPERIMENTAL METHOD

A. Apparatus for Plasma Production

The device for producing plasma has been described in several publications.[24,9,10] Studies on the technique have been reported by Brennan et al.[25] and a study of the state of a hydrogen plasma produced in an essentially identical device has been reported by Cooper.[26] The method will be reviewed here.

A cylindrical copper tube (hydromagnetic waveguide) of 14.6 cm inner diameter and 86.4 cm long is placed in a uniform dc magnetic field of 16 kG. The ends are closed with Pyrex or quartz plates, one of which (driving-end plate) holds a 5-cm-long, 5-cm-diam cylindrical molybdenum electrode concentric with the copper tube (see Fig. 8).

A base pressure of 2.5×10^{-5} torr is maintained in the tube. While an experiment is in progress, deuterium gas flows through the tube, maintaining a pressure of 80 millitorr. The deuterium pressure is monitored with a Pirani vacuum gauge, which is calibrated against an oil manometer. Deuterium was used rather than hydrogen so as to have a lower ion-cyclotron frequency, thus lowering the upper frequency limit of the experiment and making it easier to build high-Q circuits for the wave drive.

A lumped constant pulse line is charged initially to 10.5 kV and is connected to the molybdenum center electrode by an ignitron switch. The center electrode is the anode and the tube wall is the cathode. When the ignitron is fired the gas breaks down and a current of 5600 A flows between the electrode and the tube wall, ionizing the gas. The radial current, crossed with the axial magnetic field, exerts an azimuthal force on the plasma, causing the plasma to rotate. Gas in front of the rotating plasma then breaks down, and a well-defined ionization front develops and travels down the tube with a velocity of 3.9 cm/μsec. Such a phenomenon, called a "switch-on ionization wave" or hydromagnetic ionizing wave, has been investigated theoretically by Kunkel and Gross.[27]

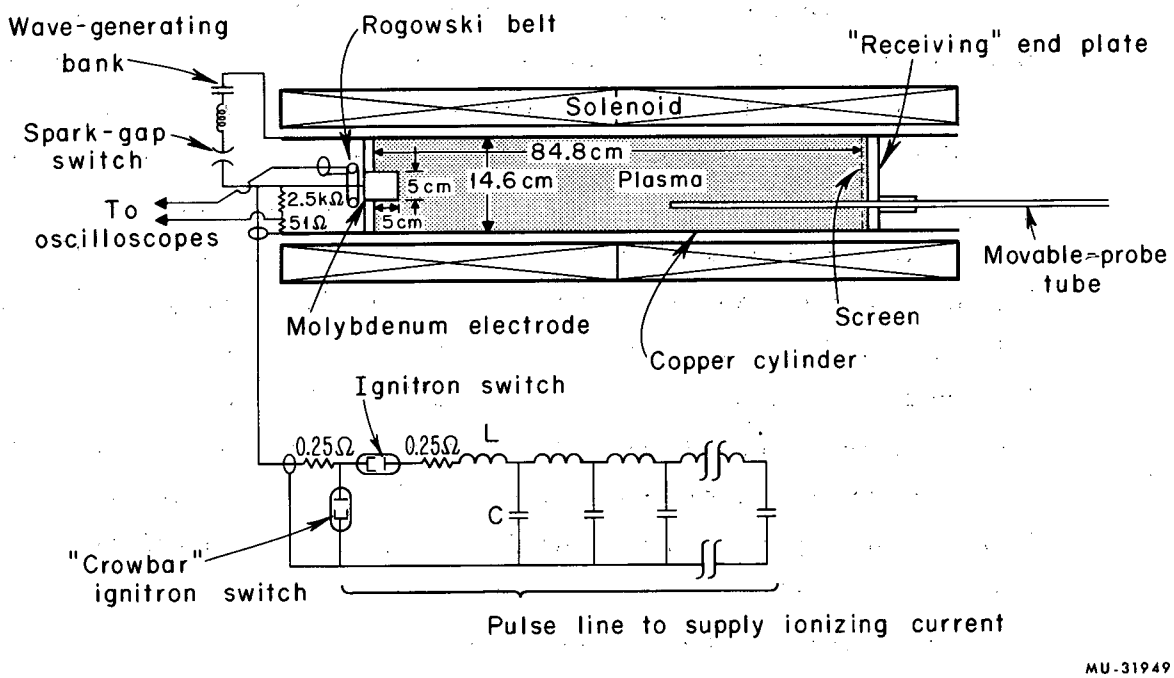

Fig. 8. Schematic of the experiment. A copper cylinder (hydromagnetic wave guide) is placed in a solenoid which produces a uniform magnetic field. Deuterium gas is ionized by discharging a pulse line between the molybdenum electrode and the copper tube wall. Waves are produced by discharging a ringing bank between the same electrodes. The electrode current and voltage are measured by displaying Rogowski-belt and resistance-divider signals on an oscilloscope. The wave is observed by a probe in the movable probe tube.

If the current continues to flow after the front reaches the receiving end, prominent spectral lines of impurities appear; therefore, the driving current is shorted ("crowbarred") before the front reaches the end of the tube. After the "crowbar," hydromagnetic "swirls" develop[28] (see Fig. 9). These swirls indicated macroscopic motion of a nonuniform plasma. To inhibit this motion, a copper screen is placed in the tube near the receiving end. This conductor constrains electric fields perpendicular to the tube axis and inhibits plasma motion perpendicular to the magnetic field (see Fig. 10).

If the current is "crowbarred" before the front reaches the screen, the tube voltage drops and the current through the electrode reverses, dissipating part of the energy of plasma rotation in the crowbar circuit. The tube voltage is measured by means of a resistance voltage divider at the tube (Fig. 8) and a 47-to-5 resistance divider at the scope input. The current is monitored by a Rogowski belt placed around the electrode external to the plasma. The current and voltage are displayed on a dual-beam oscilloscope. Typical current and voltage traces are shown in Fig. 11.

B. Spectroscopic Measurement of Plasma Properties

The radial distribution of electron temperature and density has been measured spectroscopically by using instrumentation used previously by Cooper.[26] For a general discussion of spectroscopic measurements of temperature and density in cold plasmas, see Griem.[29] We give here a brief summary of the theory of the measurements, the method and instrumentation, and results.

1. Theory

In the equations in this section we use Gaussian units.

The power radiated per unit volume in a spectroscopic line because of a transition from quantum state q to quantum state p is given by

$$I = h\nu A_{qp} n_q,$$

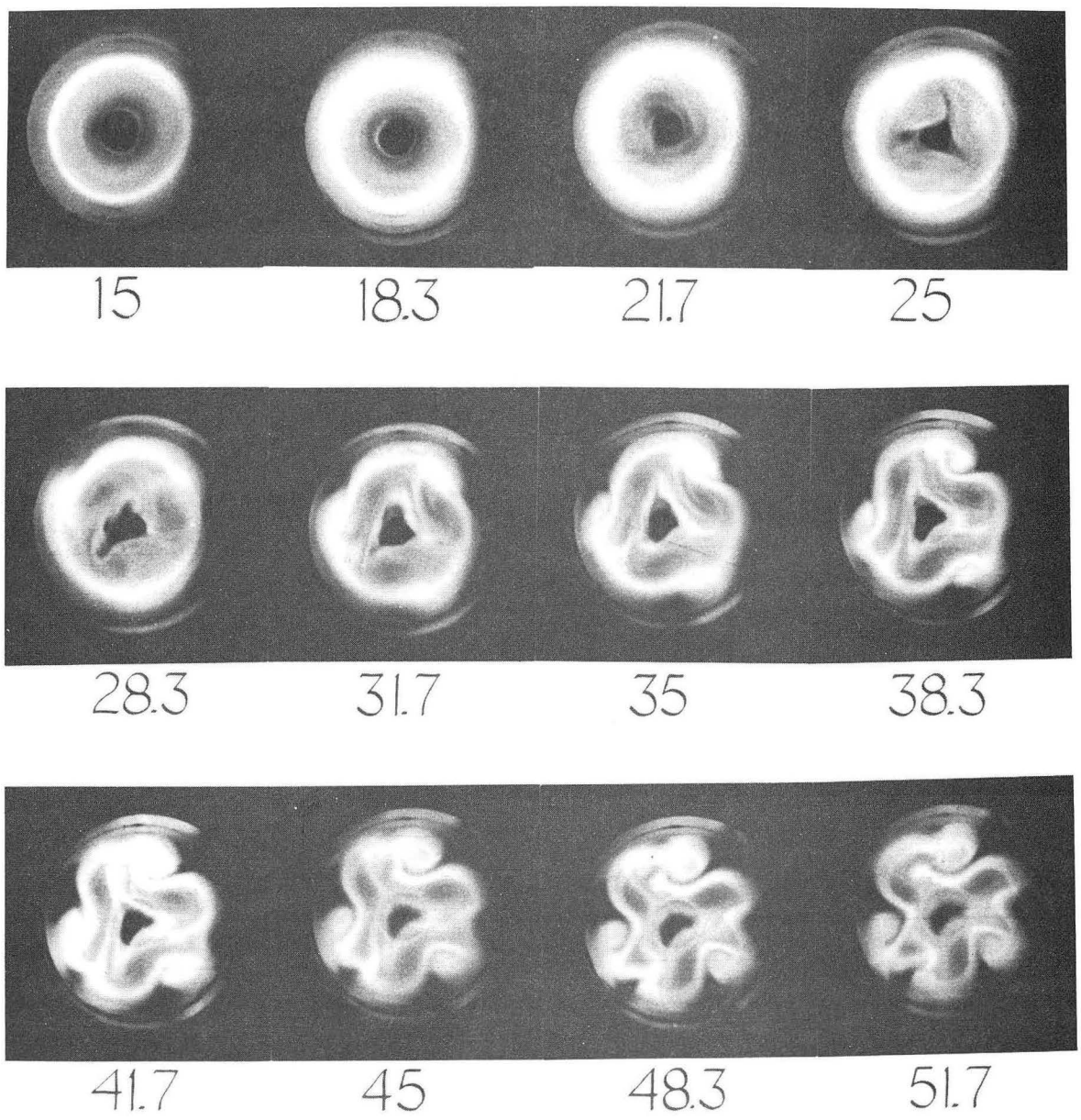

Fig. 9. A series of 12 framing-camera pictures showing "swirl" formation in a hydrogen plasma. The view is from the receiving end looking toward the driving (electrode) end. The center electrode is at positive potential for the ionizing current, and the magnetic field is directed into the paper. The time in microseconds from firing the ignitron switch of the ionizing-current pulse line is given below each frame. "Crowbar" time is about 20 μsec. There are no probe tubes in the plasma

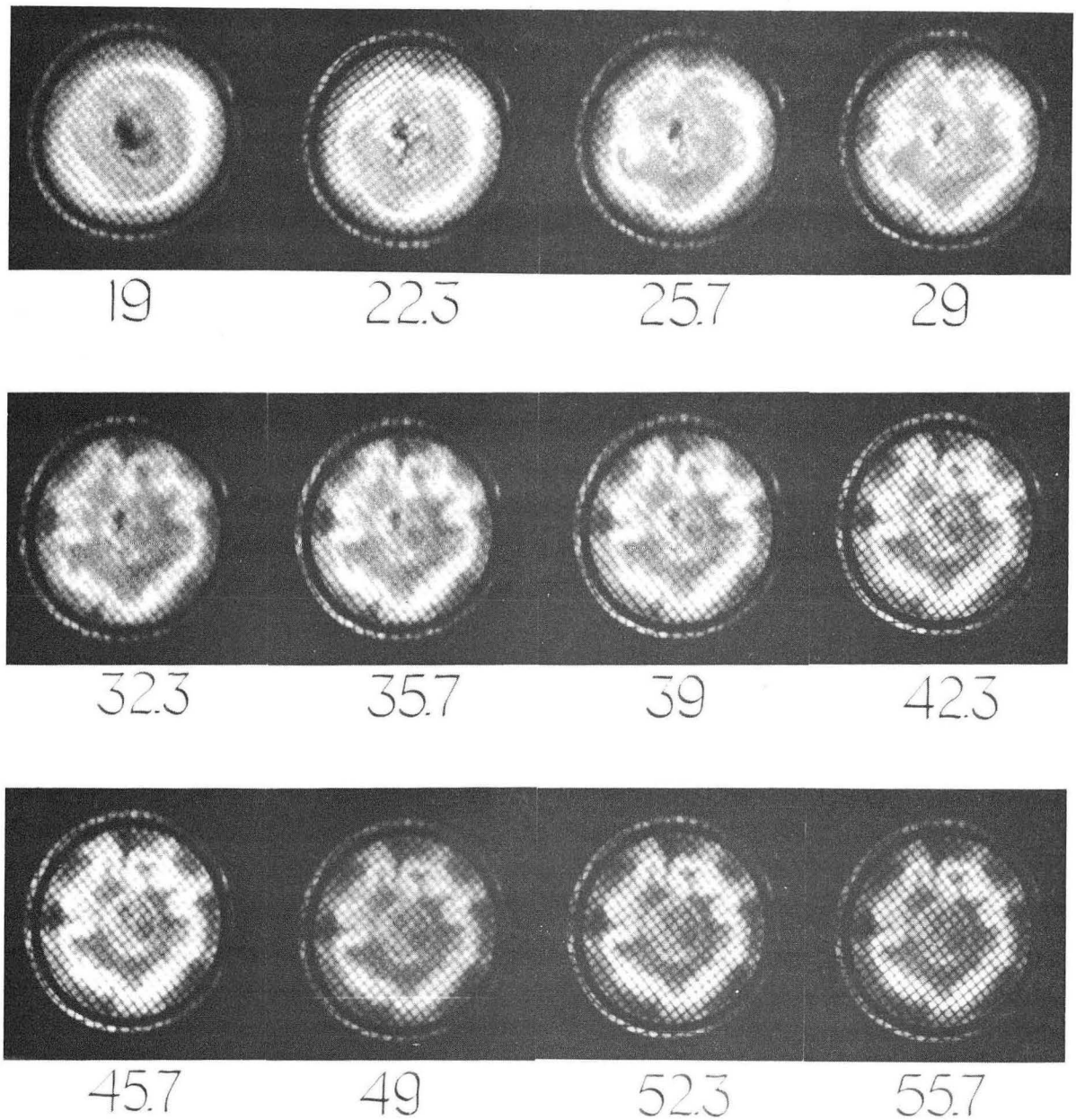

Fig. 10. Effect of conducting screen on "swirl" formation. The same conditions prevail as in Fig. 9.

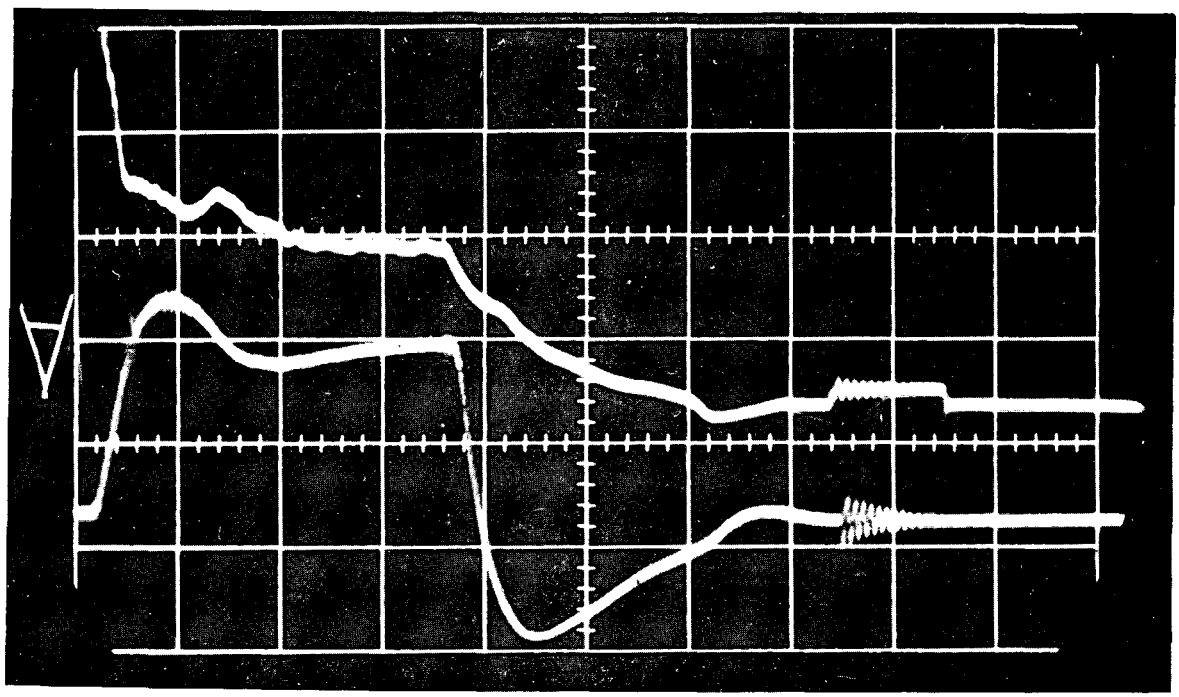

ZN-3989

Fig. 11. Voltage and current for ionizing-front and-wave oscilloscope sweep signal. The top trace is the electrode voltage at 1680 volts per large division, and the positive gate-out signal from a wave-monitoring oscilloscope. The latter is used to monitor the wave firing time and is helpful in instances whenever the wave current is too low to be easily seen on the current trace. The lower trace is the ionizing current at 3520 A per large division. The wave current may also be seen at 37 μsec. At 26 μsec one can see a small current and voltage reversal, indicating contact with the copper screen at the end of the tube.

where $h\nu$ is the quantum energy, n_q is the density of atoms in quantum level q, and A_{qp} is the probability of a transition from quantum state q to quantum state p. Stimulated emission has been neglected. The A_{qp} are known; therefore one needs only n_q.

For a sufficiently high value of q, electron collisional effects dominate radiative effects, and population and depopulation of the state are by inverse processes. In such a case the population n_q is given by the Saha equation for hydrogen

$$\frac{n_i n_e}{n_q} = \frac{2}{q^2} \frac{(2\pi m_e kT)^{3/2}}{h^3} e^{-\chi_q/kT}$$

where h is Planck's constant, k is Boltzmann's constant, T is the electron temperature (Maxwell distribution assumed), and χ_q is the ionization potential of quantum state q.

The Saha equation holds even though there is no equilibrium with radiation and though the population of the lower states may be far from that given by the equation. Combining the above results we have

$$I = h\nu A_{qp} \frac{q^2 h^3 e^{\chi_q/kT}}{2(2\pi m_e kT)^{3/2}} n_i n_e . \qquad (3.1)$$

The emission coefficient for the continuum may be derived from the classical radiation formula (Finkelnburg and Peters[30])

$$R = \frac{2e^2}{3c^3} \left(\frac{dv_e}{dt}\right)^2 .$$

By integrating R over the orbit of an electrons colliding with a nucleus of charge Ze and over impact parameters, one obtains for the radiated energy per sec and per unit frequency interval at frequency ν

$$dI_\nu(v) = \frac{32\pi^2 Z^2 e^6 n_i n_{e,v} dv}{3\sqrt{3}\, m^2 c^3 v} , \qquad (3.2)$$

where c is the velocity of light and $n_{e,v}\,dv$ is the density of electrons in the velocity range $v \pm dv/2$. No equilibrium assumptions of any kind have gone into Eq. (3.2). Equation (3.2) is frequency independent. Frequency dependence will enter through energy conservation during a transition.

We are concerned with continuum radiation due to two types of transition, free-free and free-bound (see Fig. 12). For free-free transitions we have the restriction $h\nu \leq 1/2\, mv^2$, and for free-bound transitions to the qth quantum level,

$$h\nu = \frac{1}{2} mv^2 + \chi_q .$$

In this quasi-classical treatment of free-bound transitions, we assume a hydrogen-like atom and assume that q is not distinct but is smeared over a range $dq = \pm 1/2$. For a fixed frequency we substitute the resulting value

$$dv = \frac{2(\chi_{q-\frac{1}{2}} - \chi_{q+\frac{1}{2}})}{m_e v}$$

into Eq. (3.2) and obtain

$$I_{q,\nu}(v) = \frac{2^7 \pi^4 Z^4 e^{10} n_i n_{e,v}}{3\sqrt{3}\, m_e^2 h^2 q^3 v^2}, \qquad (3.3)$$

which is the contribution to the continuum of free-bound transitions to the q level.

We now assume a Maxwellian velocity distribution for the electrons and substitute for $n_{e,v}$ in Eqs. (3.2) and (3.3). To get the total continuum at the frequency ν, we sum Eq. (3.3) over all contributing q and integrate Eq. (3.2) over the range $h\nu \geq 1/2\, mv^2$. We obtain

$$I_\nu = \frac{2^9 \pi^5 Z^4 e^{10} m_e n_e n_i e^{-h\nu/kT}}{3\sqrt{3}\, h^2 c^3 (2\pi m_e kT)^{3/2}} \left(\frac{kT}{2\chi_1} + \sum_{\chi_q < h\nu} e^{\chi_q/kT} \right).$$

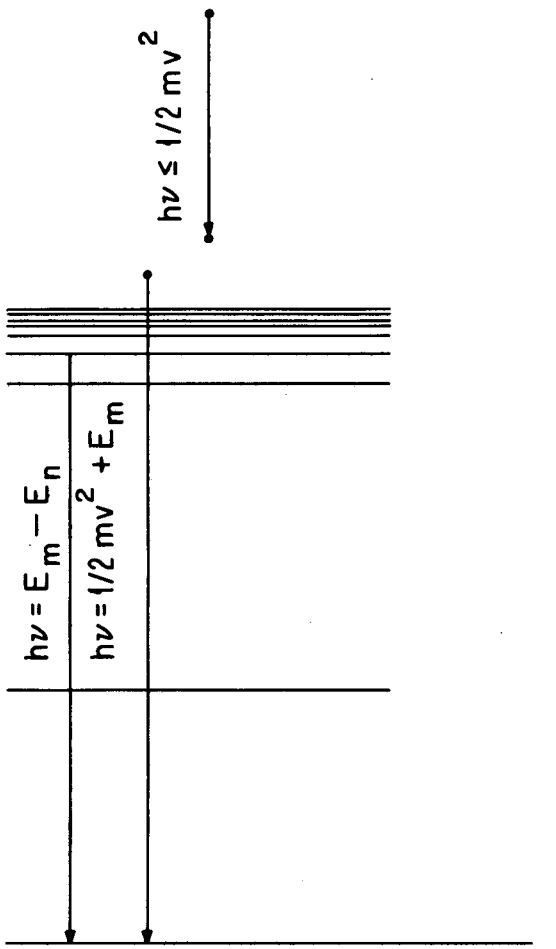

Fig. 12. Hydrogen energy-level diagram showing bound-bound, free-bound, and free-free transitions.

To provide a quantum-mechanical correction, we multiply the appropriate terms by the free-bound Gaunt factors g_{fb} and the averaged free-free Gaunt factor $\langle g_{ff} \rangle$.
We obtain

$$I_\nu = \frac{2^9 \pi^5 Z^4 e^{10} m_e n_e n_i e^{-h\nu/kT}}{3\sqrt{3}\, h^2 c^3 (2\pi m_e kT)^{3/2}} \left(\frac{\langle g_{ff} \rangle kT}{2\chi_1} + \sum_{\chi_q < h\nu} g_{fb} e^{\chi q/kT} \right). \tag{3.4}$$

From Eqs. (3.1) and (3.4) we see that a measurement of relative intensities at any two frequencies provides a temperature measurement (the $n_e n_i$ factor always cancels in any ratio). Once the temperature is obtained, an absolute calibration at one of the measured wavelengths provides a value for $n_i n_e$. We restate the two important assumptions for these measurements. (1) For measurements relying on continuum intensities, we require a Maxwellian distribution of electron velocities. (2) for measurements relying on line intensities, we require also that detailed balance hold for the upper atomic state involved in the transition (i. e., the population of the upper state is determined by Saha's equation).

In general one must worry also about contributions of the D^- continuum.[29] For the densities encountered in this experiment and temperatures greater than 10^4°K (this condition is fulfilled for measurements at all radii at wave time), the D^- continuum can be shown to be unimportant.[25] In addition, agreement between the three temperature measurements and the two density measurements are evidence that the D^- continuum can be neglected.

2. Method

The choice of wavelengths is governed by considerations such as sensitivity to temperature and density, ease of experimentation (e. g., visible and near ultraviolet are easier than vacuum ultraviolet), presence of impurity lines in the plasma and possible contribution from wings of deuterium lines, the spectral distribution of calibrating sources

available, and opportunity for internal consistency checks. In this case, the measurements were made on the D_β line, an 11.5-Å-wide continuum band at 5320 Å and a 4-Å-wide band at 3225 Å (across the Balmer series limit from 5320 Å). The intensity of the continuum band at 5320 Å is not a strong function of temperature, and hence provides a good density measurement. The density is also calculated from the intensity at 3225 Å, and the temperature is calculated from the intensity ratios $I(D_\beta)/I(5320)$, $I(D_\beta)/(3225)$, and $I(5320)/(3225)$. The latter measurement takes advantage of the temperature sensitive jump across a series limit corresponding to the addition of a new term in Eq. (3.4). Qualitative features of a deuterium plasma spectrum are shown in Fig. 13.

We define $W_c(\lambda)$ as a normalized continuum intensity $W_c \equiv [I_c(\lambda)]/(n_i n_e)$, and W_ℓ as a normalized line intensity, $W_\ell \equiv [\int I_\ell(\lambda)\, d\lambda]/(n_i n_e)$, where $I_c(\lambda)$ is the continuum intensity per angstrom, $I_\ell(\lambda)$ is the line intensity per angstrom, and the integral is over the entire line width. Plots of the appropriate $W(\lambda)$ and their ratios are shown in Figs. 14 through 18.

The experimental arrangement is shown in Fig. 19. A quartz receving-end plate is used on the tube for the spectroscopic measurements. Radiation leaving the plasma through a 3/8-in.-diam hole in the conducting screen is reflected by a mirror system and focused by a quartz lens onto the entrance slit of a Jarrell-Ash Model JA-7102 3.4-m plane-grating spectrograph. The system is accurately aligned by using a cathetometer so that the optical axis of the spectrograph is parallel to the axis of the copper tube. There are five holes in the screen at radii of 1.3, 16, 33.5, 50, and 64.5 mm.

Located in the focal plane of the spectrograph are three movable assemblies, each containing an adjustable exit slit and a mounting for a photomultiplier; EMI 6255B photomultiplier tubes are used.

To cut down on contributions due to scattered light within the spectrograph, filters are placed in front of the photomultipliers. Interference filters are used for the observations in the visible region,

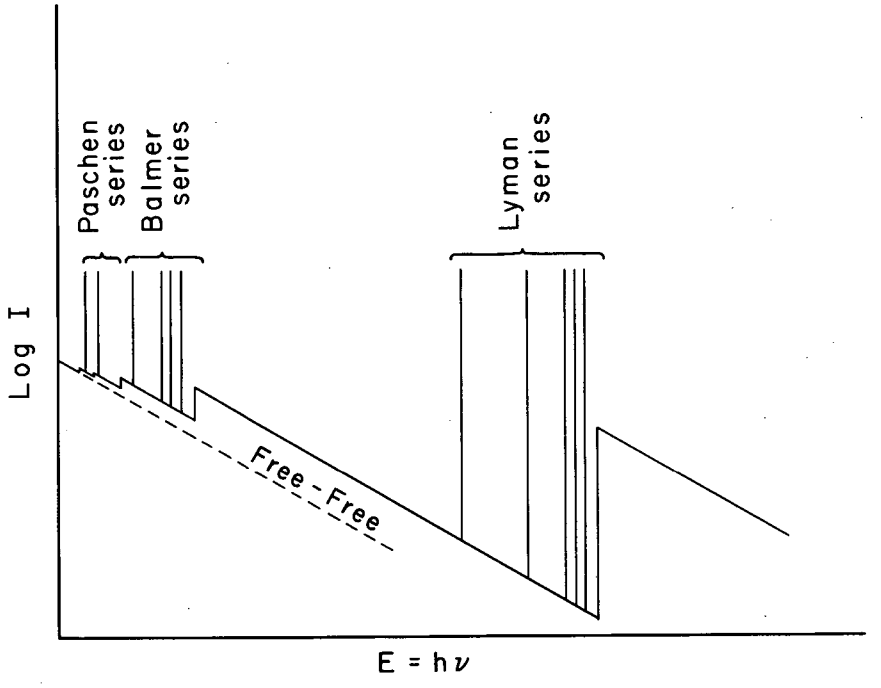

Fig. 13. Diagram of the hydrogen plasma spectrum. The dotted line, which has a slope $-h\nu/kT$, represents continuum due to free-free transitions (Bremsstrahlung). As each series limit is reached, the continuum jumps (the slope remains $-h\nu/kT$), corresponding to adding a new term in Eq. (3.4). The first few lines of the first three series are also shown.

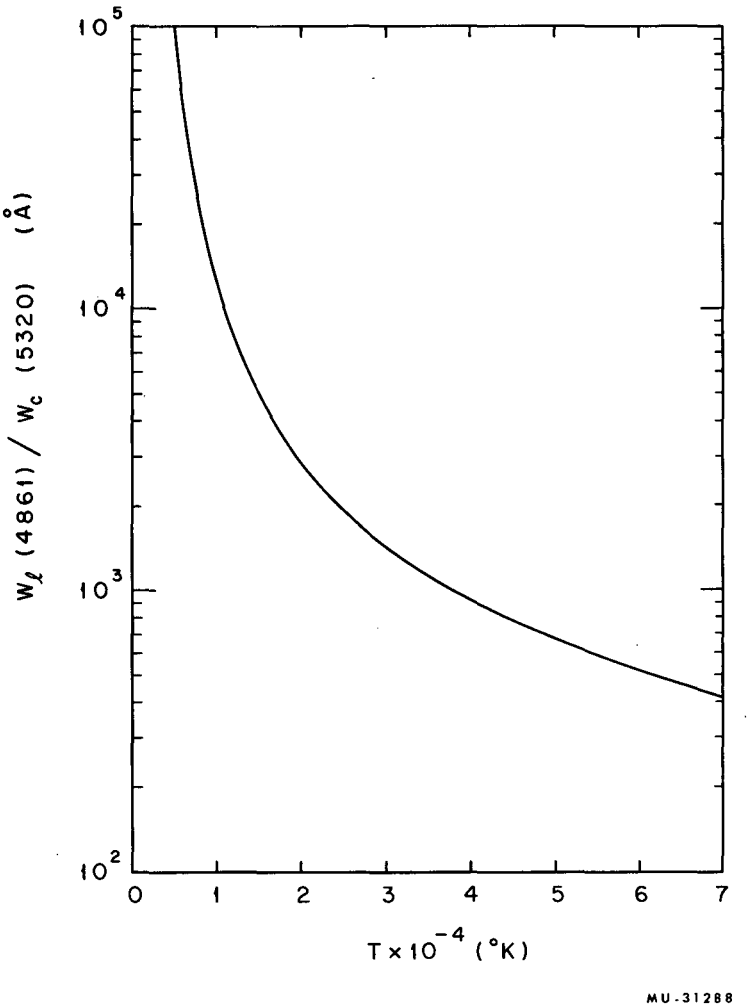

Fig. 14. Ratio of H_β line intensity to the continuum intensity per angstrom at 5320 Å as a function of electron temperature.

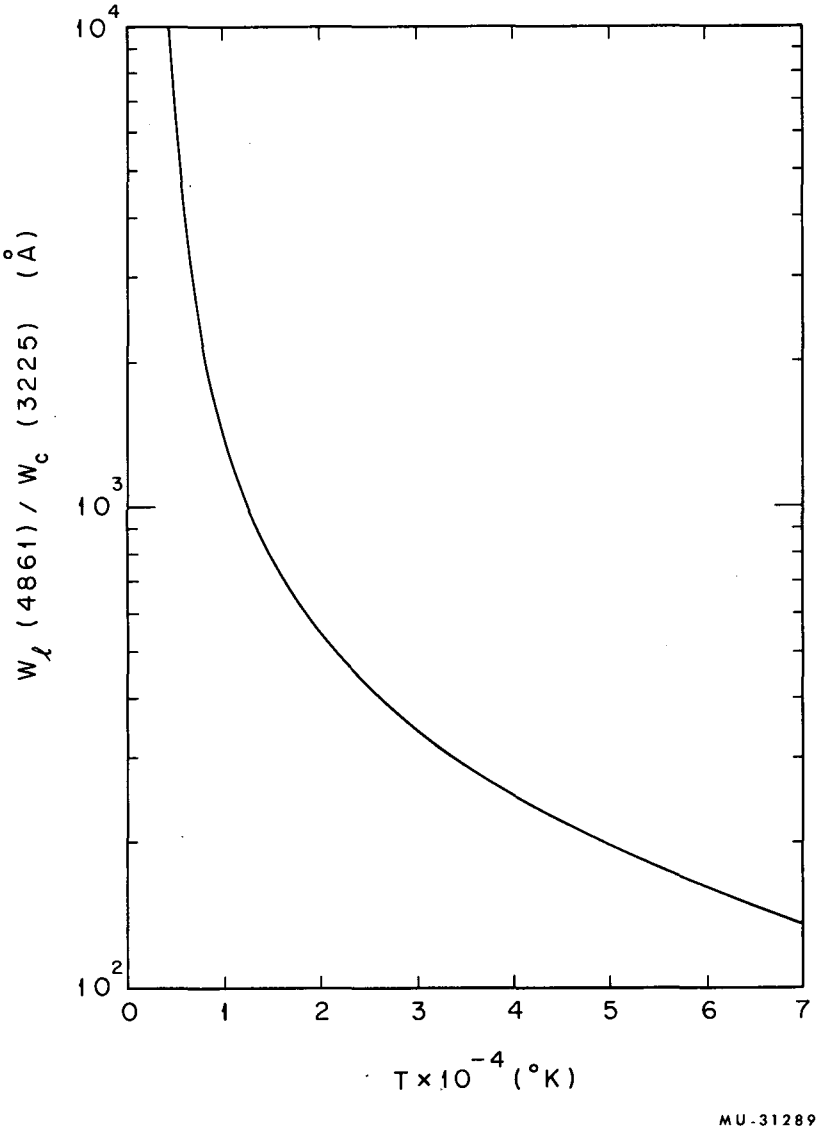

Fig. 15. Ratio of H_6 line intensity to the continuum intensity per angstrom at 3225 Å as a function of electron temperature.

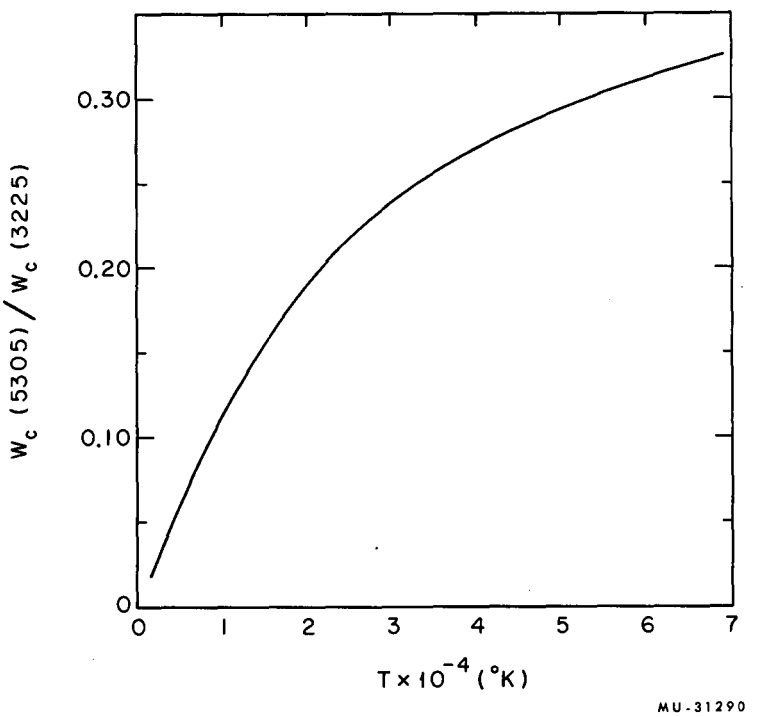

Fig. 16. Ratio of continuum intensity at 5320 Å to continuum intensity at 3225 Å as a function of electron temperature.

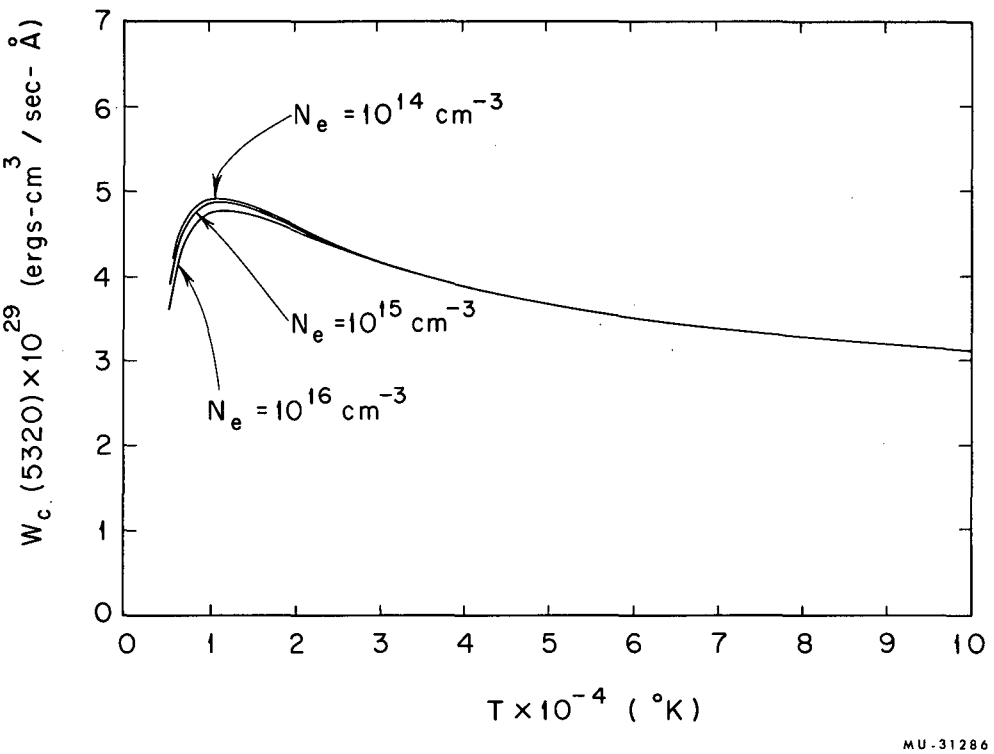

Fig. 17. Normalized continuum intensity $W_c(5320)$ at 5320 Å as a function of electron temperature.

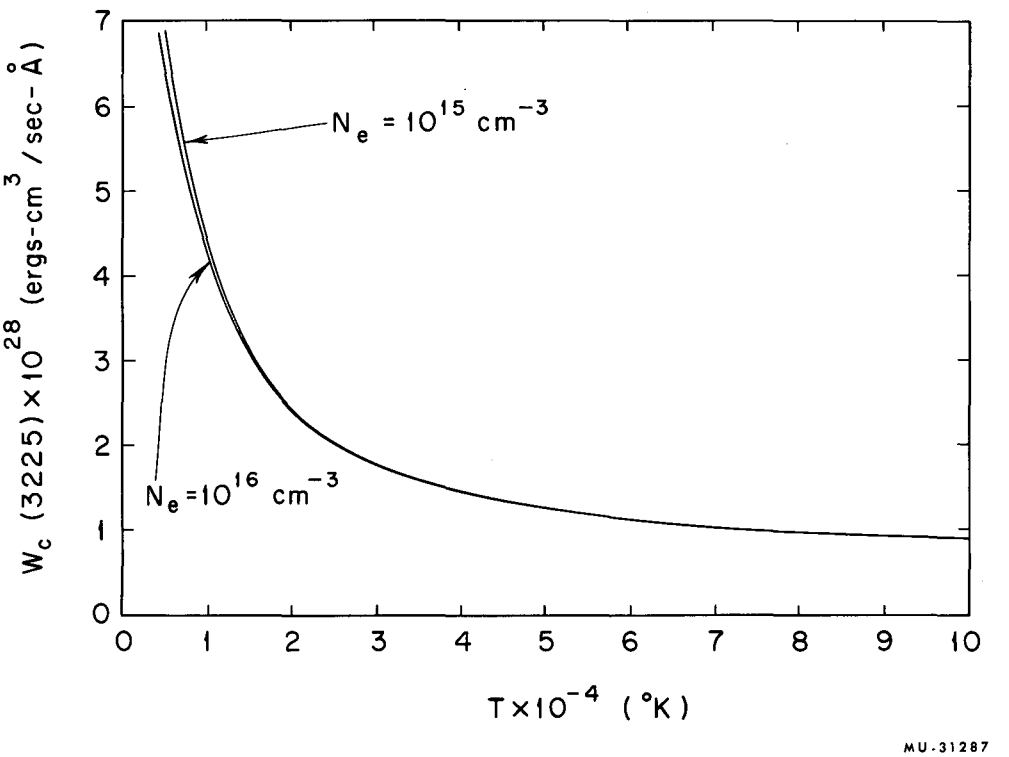

Fig. 18. Normalized continuum intensity $W_c(3225)$ at 3225 Å as a function of electron temperature.

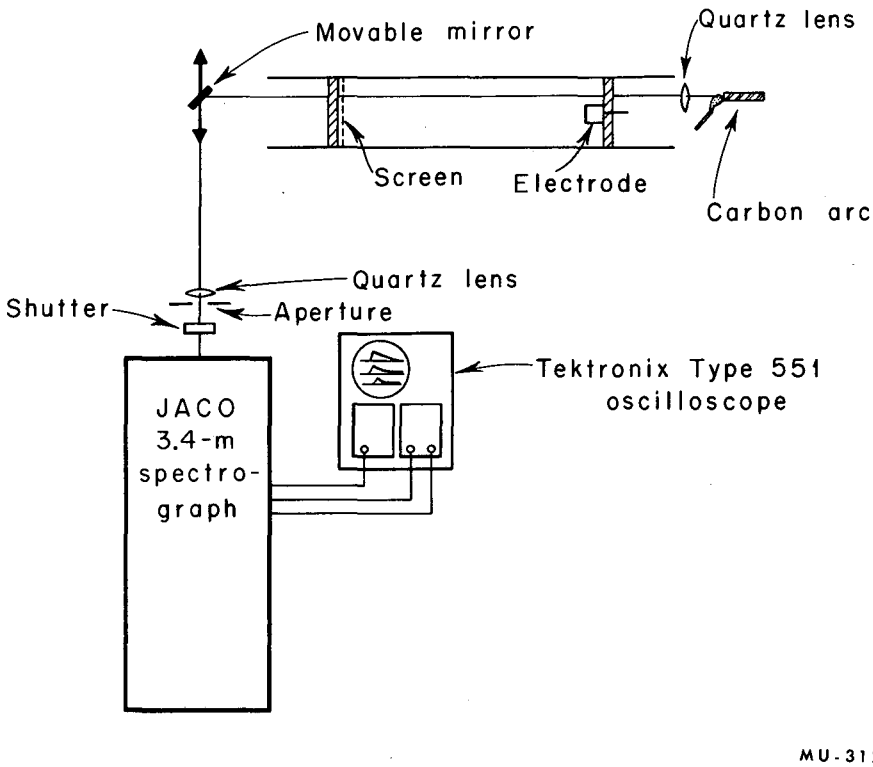

Fig. 19. Schematic diagram of the equipment used in making spectroscopic measurements.

and a Corning Type 4-76 ultraviolet filter is used for the observation at 3225 Å.

To minimize effects of drift of the gains of the photomultipliers during the course of an experiment, their gains are checked every 15 to 20 min against the output of an AR-4 argon lamp[31] mounted within the spectrograph and used as a secondary standard.

To calibrate, the end plate holding the electrode is removed from the tube and the anode spot of a carbon arc is focused on one of the holes in the conducting screen. The hole in the screen is then focused on the spectrograph slit by the quartz lens, which is already in place for focusing the plasma light onto the slit. A camera shutter is placed off-axis in front of the slit so as to give a 4-msec light pulse with a 200-μsec rise time. A light pulse is used rather than a steady source so as to avoid fatigue in the photomultipliers.

3. Results

Temperature and density profiles at the time the wave is excited are shown in Figs. 20 and 21. Each point is an average over nine shots. Error estimates (standard deviations of the set of nine shots for the D_β - 5320 Å measurements) at midradius are 6.5% in density and 4% in temperature, and near the wall are 9% in density and 3.5% in temperature. The average density according to this profile is $2.85 \times 10^{15}/cm^3$. (The density has been averaged to a maximum radius of 7 cm to correspond to the zero observed in past measurements of radial distribution of the wave field.[10]) The estimated error in the average due to lack of detailed knowledge of the sharply declining portion of the profile near the wall is 10%.

To illustrate the general agreement between measurements by various ratios, the temperature and density as measured by each ratio are presented as a function of time for a radius of 3.35 cm (Figs. 22 and 23).

To provide a further check on the density measurements, Cooper compared measurements of the Stark broadening of the H_β line with continuum measurements at 5320 Å and found agreement within

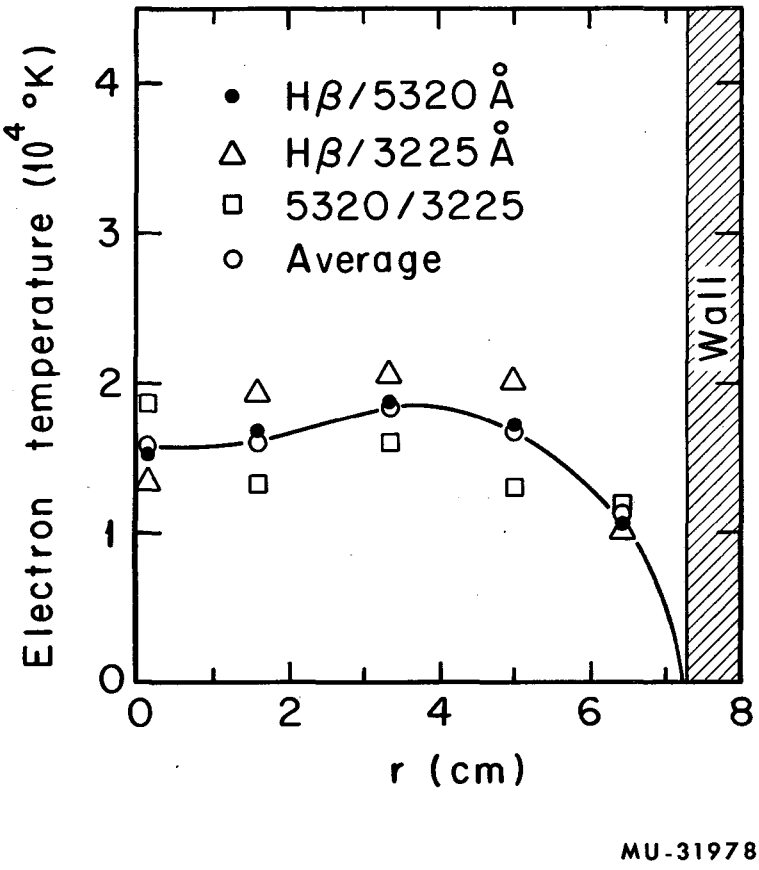

Fig. 20. Electron temperature as a function of radius as determined at wave time from measurements of the various ratios of line and continuum intensity.

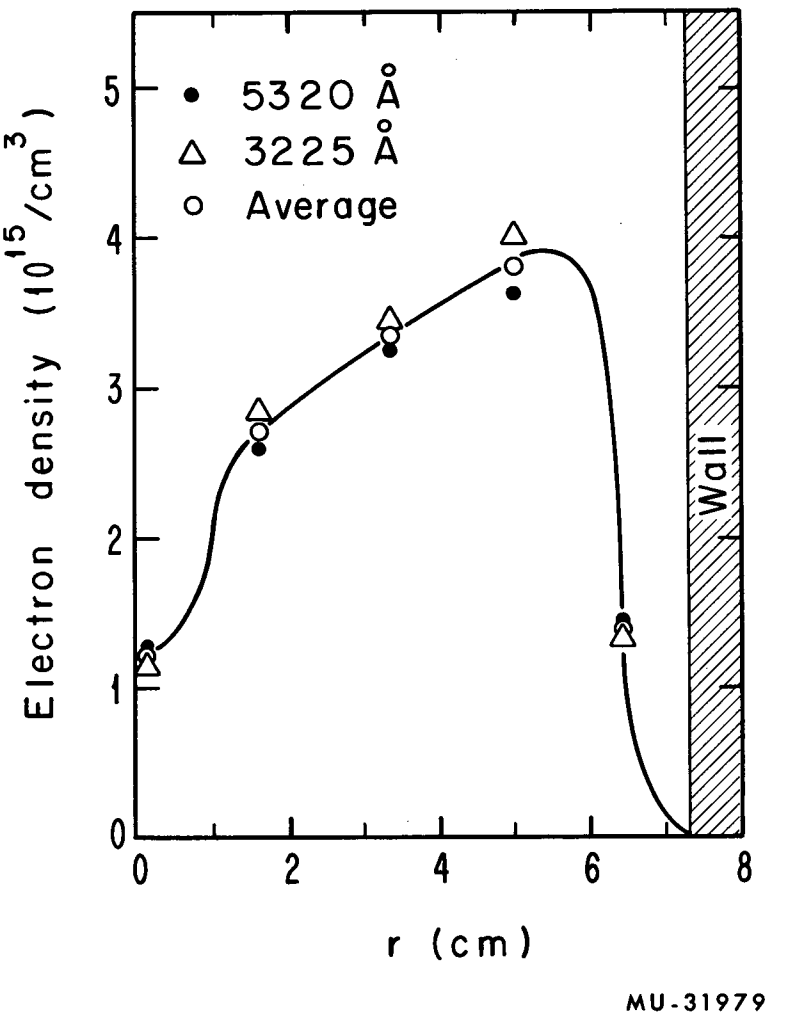

Fig. 21. Electron density as a function of radius as determined at wave time from measurements of the intensity of the continuum at 5320 Å and 3225 Å.

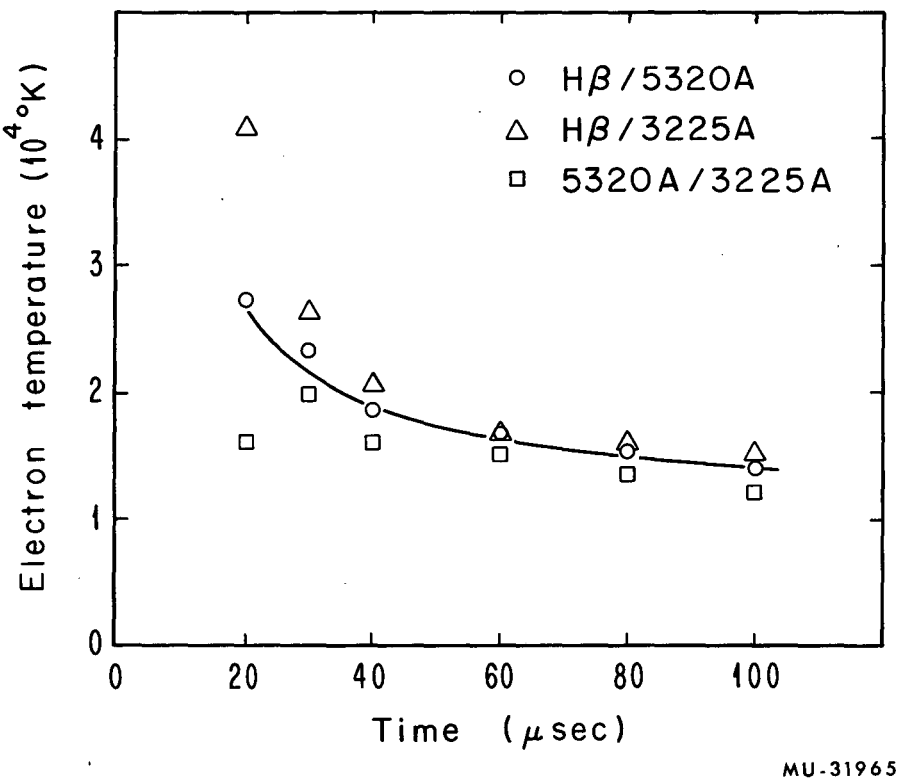

Fig. 22. Electron temperature as a function of time as determined from the three intensity ratios. All measurements are at 3.35-cm radius.

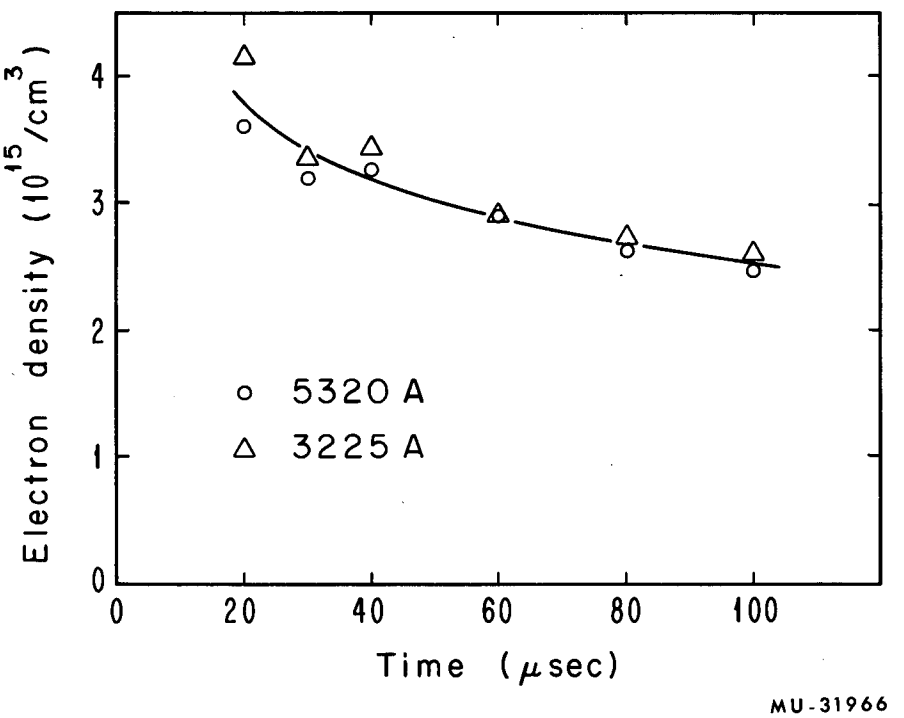

Fig. 23. Electron density as a function of time as determined from the two continuum-band intensities. All measurements are at 3.35-cm radius.

experimental errors.[26] The H_β profile was measured with an 18-channel polychromator which measures intensities as a function of time at 18 different wavelengths on the spectral line simultaneously. For a description of the instrument see Spillman et al.[32,33]

No attempt has been made on the plasma of this experiment to measure longitudinal inhomogeneity spectroscopically. It is expected the results would be essentially the same as those found by Cooper.[26] His results on longitudinal variation of density are shown in Fig. 24.

It has also been shown by Cooper that initially the ionization is essentially complete. In all theoretical curves of wave quantities (with one exception for comparison in Fig. 32), we assume therefore that no neutral particles are present.

C. Wave Excitation

The waves are excited by a discharge between the same electrodes use for the ionizing current (See Fig. 8). The discharge is from a bank built onto the end of the tube and connected by a coaxial lead to the electrodes (see Fig. 4). A spark-gap switch connects the center electrode through an inductance to the bank of capacitors, which are placed around the spark gap at a radius of about 10 cm.

The capacitors used in all experiments, except those reported in the Appendix on a surface wave, were Plastic Capacitors, Inc. HG 250-501, 500-pF, 25-kvdcw capacitors. The frequency was varied by changing the number of capacitors and (or) the inductance in the bank. From one (at 14.5 Mc) to 18 capacitors were used.

The maximum wave current used for the dispersion measurements was 1470 A, providing a maximum wave magnetic field (at the center electrode) of 118 G. This corresponds to a maximum perturbation ratio of 7.4×10^{-3} on the static uniform field.

Because of distortion of the wave train due to dispersion and attenuation of the higher frequencies, it is desirable to have a high-Q circuit for exciting a wave train of many cycles. We consider building a bank of N_p parallel units of N_s capacitors in series. We assume each capacitor to have a capacitance C and a loss due to an equivalent

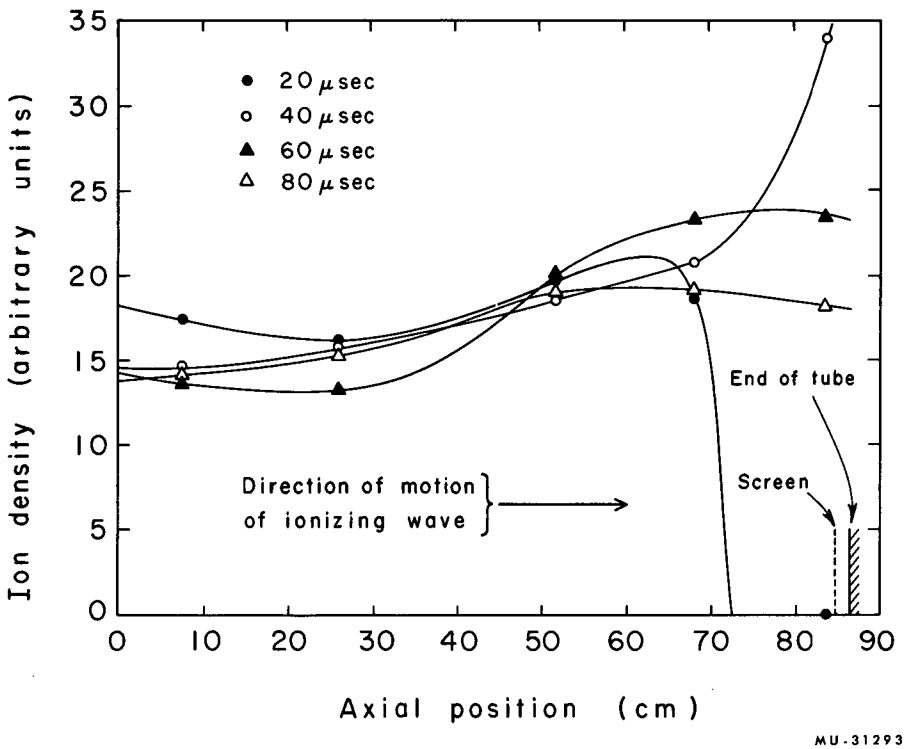

Fig. 24. Cooper's[25] results on longitudinal variation of density in hydrogen plasma. The curve at 40 μsec should correspond most nearly to the conditions at wave time in this experiment.

resistance R_c. We may then write for the Q of the circuit

$$Q = \frac{1}{[Z_p(N_p/N_s) + R_c]\omega C},$$

where Z_p is the plasma hydromagnetic impedance. We have neglected losses other than those in the plasma or the capacitors. Therefore an optimum bank has $Z_p(N_p/N_s) << R_c$, subject of course to the condition that sufficient current is also obtainable from the bank. In all instances in this experiment, we have $N_s = 1$. Experiments at lower density (higher Z_p) make $N_s > 1$ desirable. The measured Q for the highest frequency at which dispersion measurements were made is 18. The measured low-frequency plasma hydromagnetic impedance is 0.1Ω.

The wave current is measured by the same Rogowski belt around the electrode that is used to measure the ionizing current. The belt has a measured inductance of 4×10^{-8} H, which is low enough not to introduce significant phase shifts at experimental frequencies.

D. Wave Measurements

1. Probes and Associated Equipment

The principal detector used in this experiment (for all attenuation and velocity measurements) is a three-coil probe with coils orthogonal to one another capable of measuring b_r, b_θ, and b_z simultaneously. Eight-turn double-layer coils are wound on identical 0.095-in.-diam bobbins. The coil leads are twisted, and each pair is carried back outside the hydromagnetic waveguide through its own solid copper shield, where the coil leads connect to coaxial cables going to oscilloscopes in a screenhouse. Shields from the screenhouse cover the oscilloscope cables and connect to the probe shields, effectively extending the screenhouse to the vicinity of the probe coils. The coils themselves are not shielded, so as to avoid the possibility of effectively changing coil orientation. The distance between centers of coils is 3.3 mm. We identify coils, starting from outermost tip, as No. 2, No. 3, and No. 1. The axis of No. 3 coincides with the probe axis (b_z coil).

The probe was tested in a probe calibrator which consisted of two parallel straps through which a capacitor was discharged. Cross talk between coil No. 2 and the other coils was negligible. Cross talk from coil No. 3 onto No. 1 was 3% at 1.8 Mc. Cross talk from No. 1 onto No. 3 was 2% at 1.8 Mc, 1.4% at 14.2 Mc. Coils No. 1 and No. 2 (b_r and b_θ) were found to be orthogonal to within less than 0.2 deg. No. 1 and No. 3 and coils No. 2 and No. 3 were found to be orthogonal to within 1.2 deg (these last measurements were limited by the cross talk between coils No. 1 and No. 3).

The No. 2 coil was used for all dispersion measurements reported here. Other probes used were single-coil probes of four turns on a 0.094-in.-diam bobbin. Shielding was similar to that for the three-coil probe.

The probes were placed in 6.3-mm-o.d. quartz tubes entering the hydromagnetic waveguide parallel to the cylinder axis from the receiving-end plate (Fig. 8). The probe tubes were movable along the axis and could pivot a small amount at the end plate.

2. Method of Measuring Amplitudes and Times of Arrival

The derivatives of the wave current as measured by the Rogowski belt and of the wave field as measured by the probe were displayed on a Tektronix Type 551-dual-beam oscilloscope. Since the excitation is not a pure sine wave (see Fig. 25 for the spectrum of the driving current), frequencies other than the fundamental were present. Because the higher frequencies are more rapidly damped, it seems more desirable to observe time derivatives of the wave magnetic field rather than the field itself. This gives a higher weighting to higher frequencies and is also a simplification, eliminating the need for integrators on probe and current signals.

Because of the dispersion- and frequency-dependent attenuation, the wave form becomes distorted as the waves move down the tube. It is observed that late in the wave train the form is the same as the driving signal, and then is a sufficiently accurate approximation to a pure sine wave. The number of peaks are counted from the beginning of the wave signal to the point in the wave train at which measurements

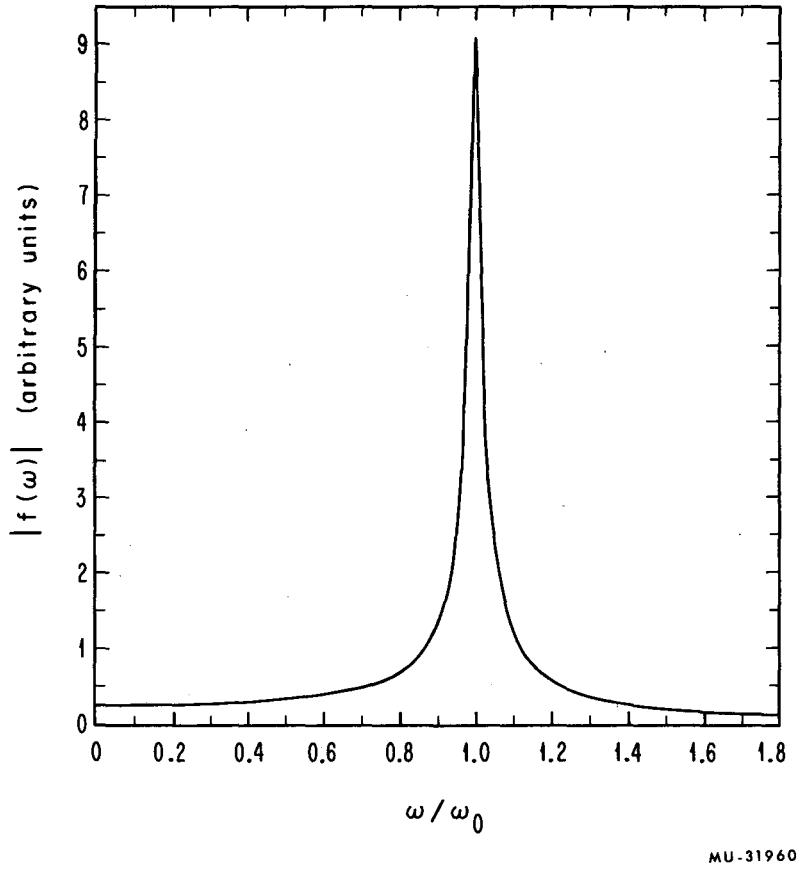

Fig. 25. Frequency distribution of a damped sine wave from a circuit having Q=18. The fundamental frequency is taken as ω_0.

are to be made, and the time of transit is measured as the difference between this wave peak and the corresponding peak in the current. This varied from the second peak (first cycle) at 485 kc to the tenth peak (fifth cycle) at 5.87 Mc.

To avoid possible error due to a shift in the base line, amplitudes were measured from a positive peak (same one on which time of arrival is measured) to the next (negative) peak, exception at 485 kc. There it was necessary to measure from the second peak to the base line because reflections interfered with the third peak.

3. Choice of Radial and Axial Positions, Wave Time, and Crowbar Time

Earlier measurements than those reported in the results section of this thesis were made at a larger radius. Plots of the logarithm of the wave amplitude versus axial position showed a greater attenuation close to the driving end than further down the tube. This suggested that part of the observed amplitude close to the driving end was due to higher, more attenuated radial modes. To minimize effects of higher modes, we considered it desirable to place the probe near the zero of the second mode (3.75 cm for a plasma radius of 7 cm). Another desirable feature would be to have the probe near the maximum of the first mode (3.56 cm for a plasma radius of 7 cm), so that small variations in radius would have negligible effect on the measured amplitude. A radius of 3.55 cm was chosen. At this radius the ratio of the first to second mode at the wave exciter is calculated to be 161.

Axial positions for measurements are limited near the receving end by reflections and near the driving end by probe perturbations of the plasma. This is discussed further in the section on experimental results.

A crowbar time was chosen at which the scatter in wave-amplitude measurements was less than for other crowbar times that were tried. Similarly, the chosen wave time resulted in less scatter than later wave times. Serious perturbations to the wave signal would occur at earlier wave times because of the crowbar current.

4. General Procedure for Wave Measurements

The three-coil probe, which was used for all velocity and attenuation measurements, was placed in a movable axial probe tube, and the radial position was checked carefully with a cathetometer. The

probe was always pushed all the way into the probe tube, and the outermost coil was used to make time-of-arrival and amplitude measurements of db_θ/dt.

Drooping of the probe tube was not eliminated; rather the effect of drooping on changing probe-coil orientation was corrected by rotating the probe to minimize b_r/b_θ at 485 kc/sec. This rotation was at most an 8-deg correction.

After the position and orientation of the probe was set and checked, fifteen shots were taken at each frequency, and the probe and probe tube were moved to a new axial position and the procedure was repeated. On some of the measurements, another probe was placed near the receiving end to monitor the time of arrival and wave amplitude at a fixed position.

The db_θ/dt signal and the dI/dt signal measured by the Rogowski belt were displayed on a Tektronix 551 oscilloscope. To allow relative phase measurements between db_θ/dt and db_r/dt, these signals were displayed on a delayed fast sweep on another Tektronix 551 oscilloscope. The delay was such that the displayed signal was in the regular portion of the wave train (i.e., after the wave appeared to achieve the form of a damped sine wave). In some cases these signals were also displayed on a slower sweep speed such that distortions in the early part of the wave train could be observed.

The firing time of the wave-generating bank was monitored by displaying the sweep signal of one of the wave oscilloscopes with the ionizing current and voltage signals on a Tektronix 555 oscilloscope (see Fig. 11). The wave oscilloscopes (with the exception of the one delayed sweep) were triggered from the signal of a Rogowski belt placed inside the wave-generating bank.

IV. EXPERIMENTAL RESULTS

A. Wave Velocity

The wave velocity was measured by measuring the arrival time of some particular peak in the wave train (Section III-D-2) at a number of axial positions. Plots of time of arrival vs axial position for three frequencies are shown in Figs. 26 and 27.

A general character was noted for such plots. The points from 37.3 to 60.3 cm fit straight lines, whereas points closer to the driving end were later in time than would be expected from the straight-line fit. This was true except for the lowest frequency (0.485 Mc/sec).

This deviation of the close-in points from the straight line increased with frequency. Accordingly, the velocity and its estimated error were calculated by fitting a straight line to the points from 37.3 to 60.3 cm by the method of least squares.

We may note another general characteristic of the time-of-arrival plots which is related to that mentioned above. The least-squares-fitted lines do not pass through the origin. With the exception at 0.485 Mc/sec, they all have positive axial position intercepts (i.e., they appear to start at some distance down the tube from the driving-end plate). These intercepts are plotted vs frequency in Fig. 28.

From Fig. 28 we see that the intercepts tend toward zero for low frequencies except at 0.485 Mc/sec. For the latter we may draw a line (dashed line of Fig. 26) through the origin which fits all the points quite well except the two at 48.9 cm and 60.3 cm. The worst deviation is at 60.3 cm and corresponds to an error of less than 3 deg in determining the position of the peak. Such an error could result from a 2% perturbation near the peak, due perhaps to the reflection of a precursor signal too small to significantly alter the peak amplitude.

The velocities and errors as calculated by a least-square fitting to the points 37.3 through 60.3 cm are shown in Fig. 29. The point at 0.485 Mc/sec as determined by the dashed line of Fig. 26 and theoretical curves for the spectroscopically measured average ion density and two other ion densities are also shown in Fig. 29. If we take as correct the

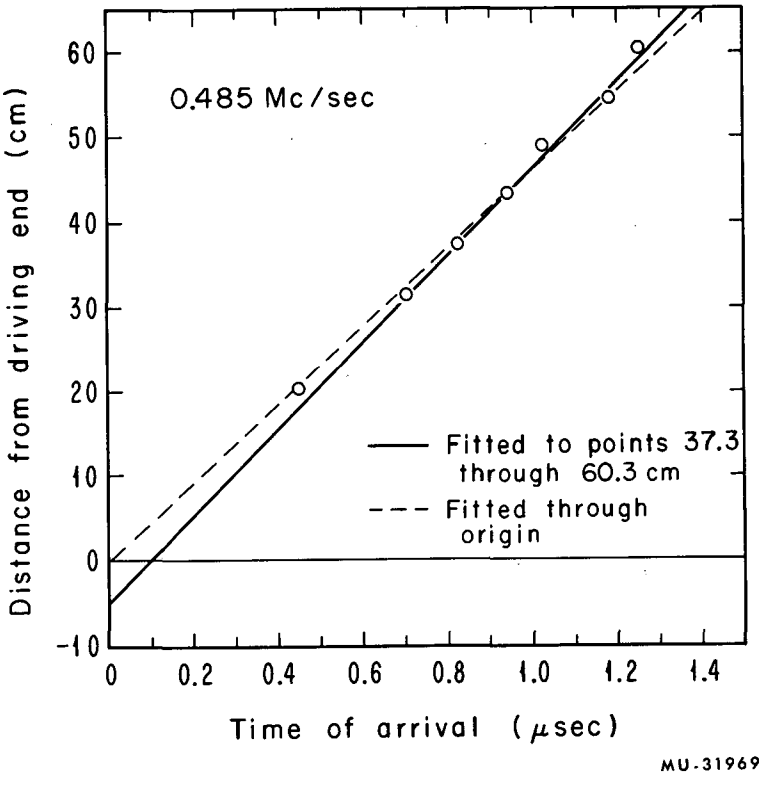

Fig. 26. Time of arrival versus axial position at 0.485 Mc/sec. The solid line is a least-squares fit to the points from 37.3cm through 60.3 cm. The dashed line is a graphical fit to the origin and all experimental points. Each point is the average of data from 15 shots.

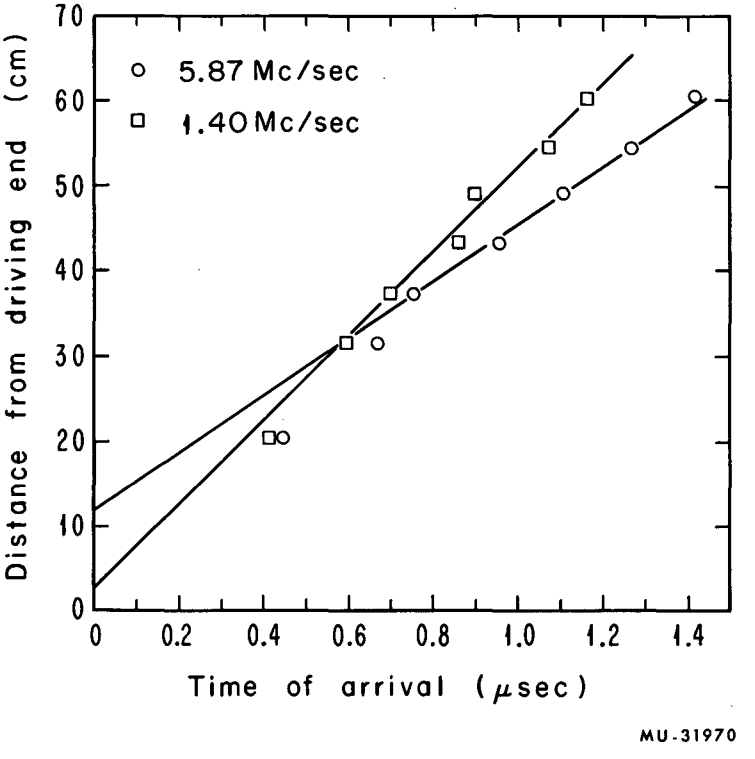

Fig. 27. Time of arrival versus axial position at 5.87 Mc/sec and 1.40 Mc/sec. The lines are least-squares fits to the points from 37.3 cm through 60.3 cm. Each point is the average of data from 15 shots.

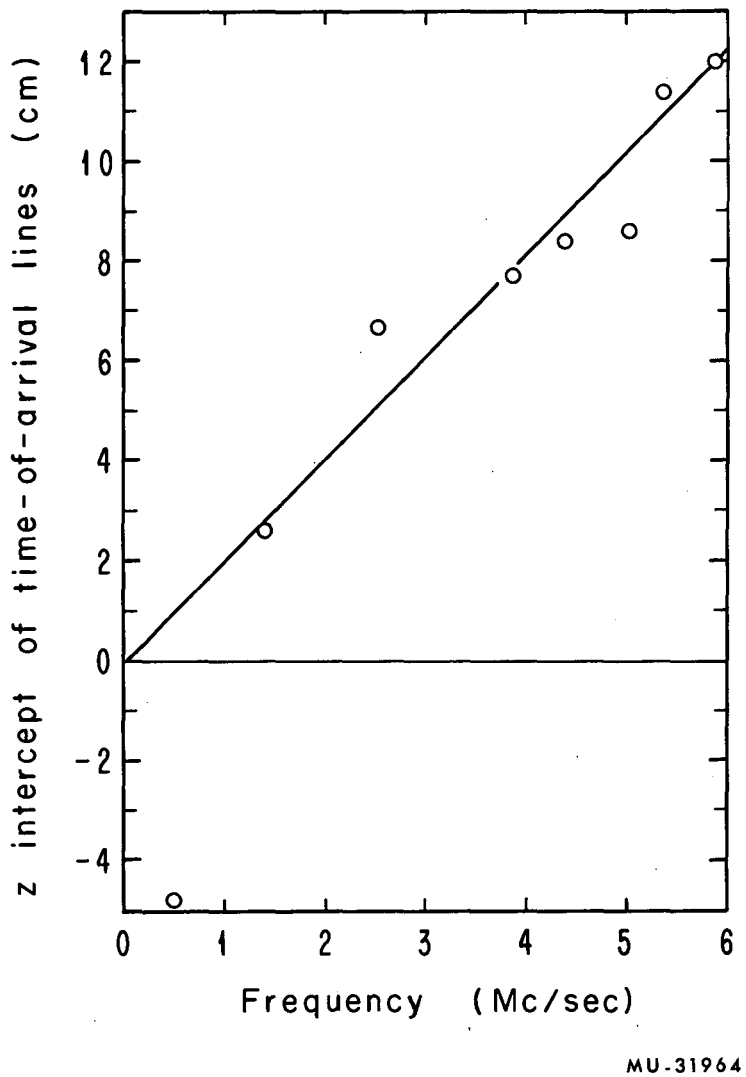

Fig. 28. The z (axial-position) intercept of the least-squares fitted lines such as shown in Fig. 27.

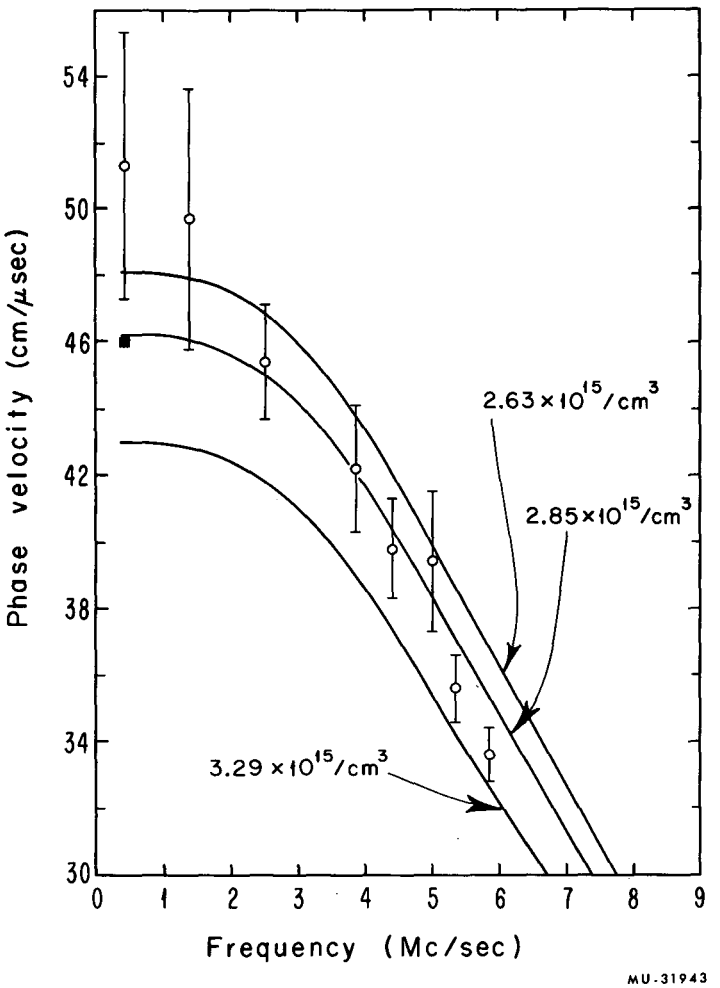

Fig. 29. Phase velocity vs frequency. The circles are velocity and the bars are estimated errors as calculated by the method of least mean squares. The square at 0.485 Mc/sec corresponds to the dashed line of Fig. 26. Theoretical curves are shown for the spectroscopically measured average ion density ($2.85 \times 10^{15}/cm^3$) and two other ion densities. For the theoretical curves, we assume a plasma radius of 7 cm and the first Bessel mode and no neutral particles. In the frequency range shown above, the theoretical curves are not significantly different for temperatures greater than 10^4 °K.

velocity corresponding to the dashed line through the origin of Fig. 26, we see that good agreement with the theoretical velocity is obtained.

B. Wave Attenuation

Wave amplitudes were measured as described in Section III-D-2. These amplitudes were normalized to the driving current and plotted vs axial position on semi-log paper. The points from 31.4 cm through 60.3 cm scattered about a straight line, except that in every case other than 5.03 Mc/sec, one point (not always the same axial position) fell far off the line (see e. g. Fig. 30). The apparently bad point at each frequency was dropped, and a best-fit straight line was chosen by the method of least squares. Experimental points with the calculated best-fit lines are shown for a low and a high frequency in Fig. 30 and 31.

The attenuation length was calculated as the reciprocal of the slope of the line, which was chosen as discussed above. The resulting attenuation lengths are plotted together with theoretical curves in Fig. 32. Errors were calculated for the least-squares fit; however, they are probably not meaningful except at the higher frequencies, because the error calculation does not take into account the dropping of a point, and the scatter of the measured attenuation length about the theoretical curves is generally large compared to the calculated errors. The point at the highest frequency (5.87 Mc/sec) is somewhat questionable because of the presence of the compressional mode, as is discussed in the next section.

The attenuation measurements are poorer than the velocity measurements. We may see, however, that the points generally scatter around a theoretical curve for 100% ionization and a temperature of about 1.25×10^4 °K. This is in reasonable agreement with the spectroscopically measured temperature (Fig. 20).

A theoretical curve for 90% ionization is also shown in Fig. 32. The charge-exchange cross section (5.7×10^{-15} cm^2) assumed by DeSilva[10] was used for calculating the curve. The large disagreement between this curve and the experimental data may be taken as additional evidence of the absence of neutral particles in the plasma at the wave time.

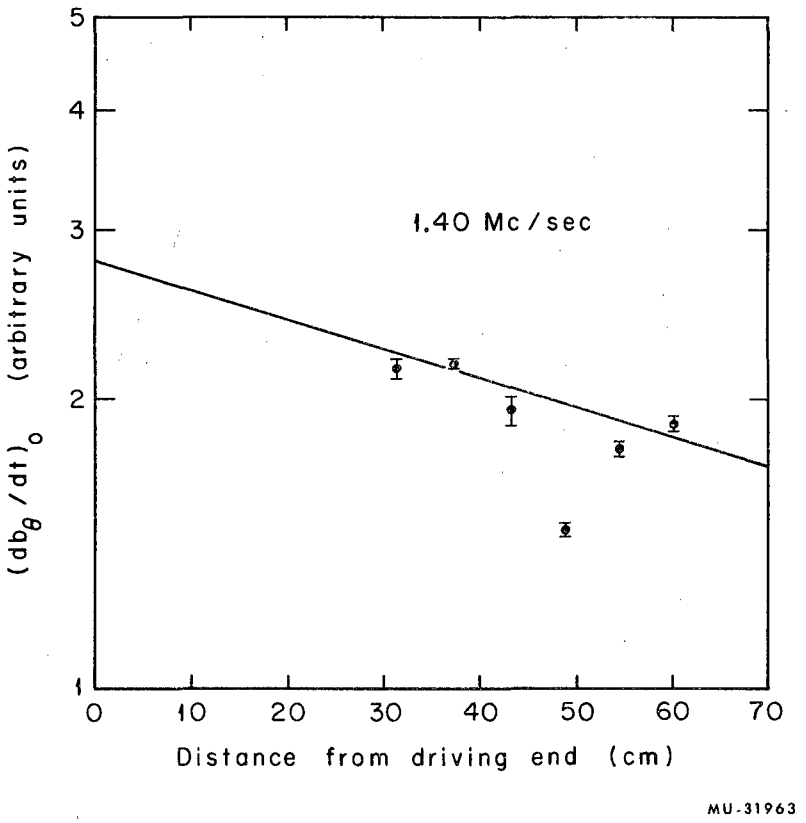

Fig. 30. Wave amplitude versus axial position for 1.40 Mc/sec. The amplitude $(db_\theta/dt)_0$ is measured as described in Section III-D-2. Bars denote standard deviations for a set of measurements. Each point is an average for 15 shots. The line is fitted to the points, except the one at 48.9 cm, by the method of least mean squares.

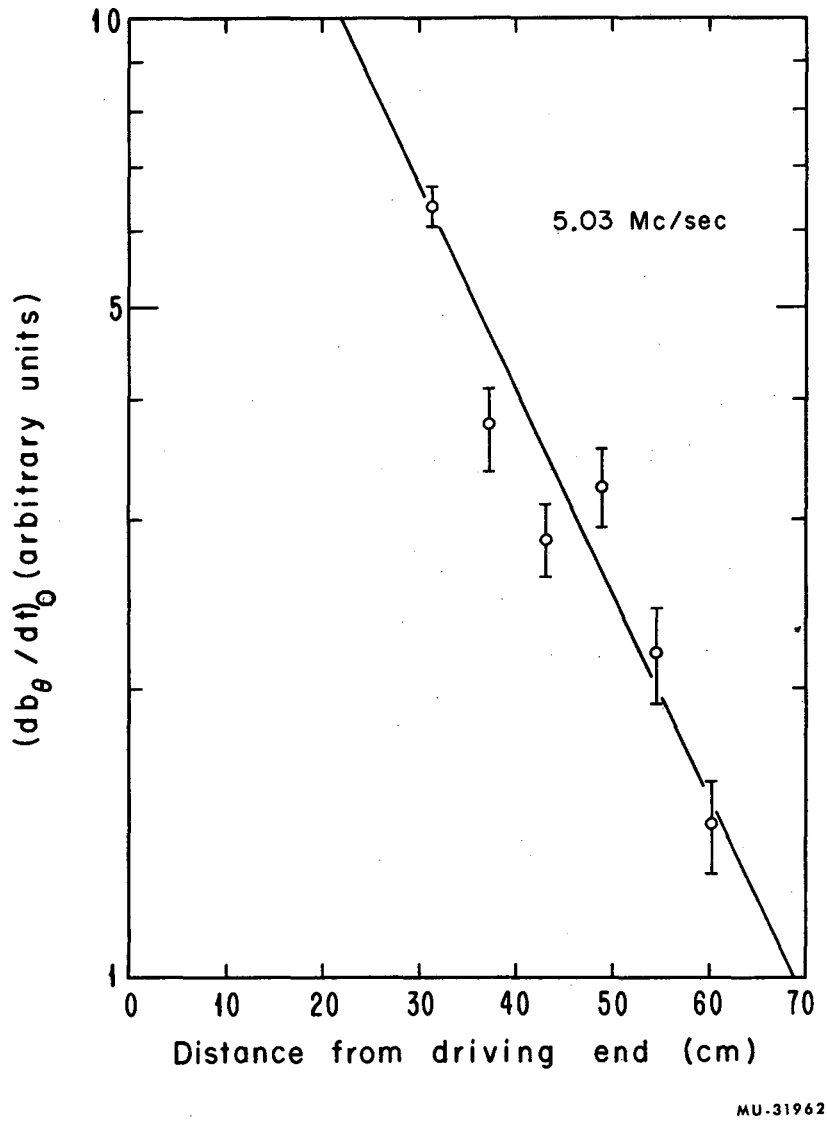

Fig. 31. Wave amplitude versus axial position for 5.03 Mc/sec.

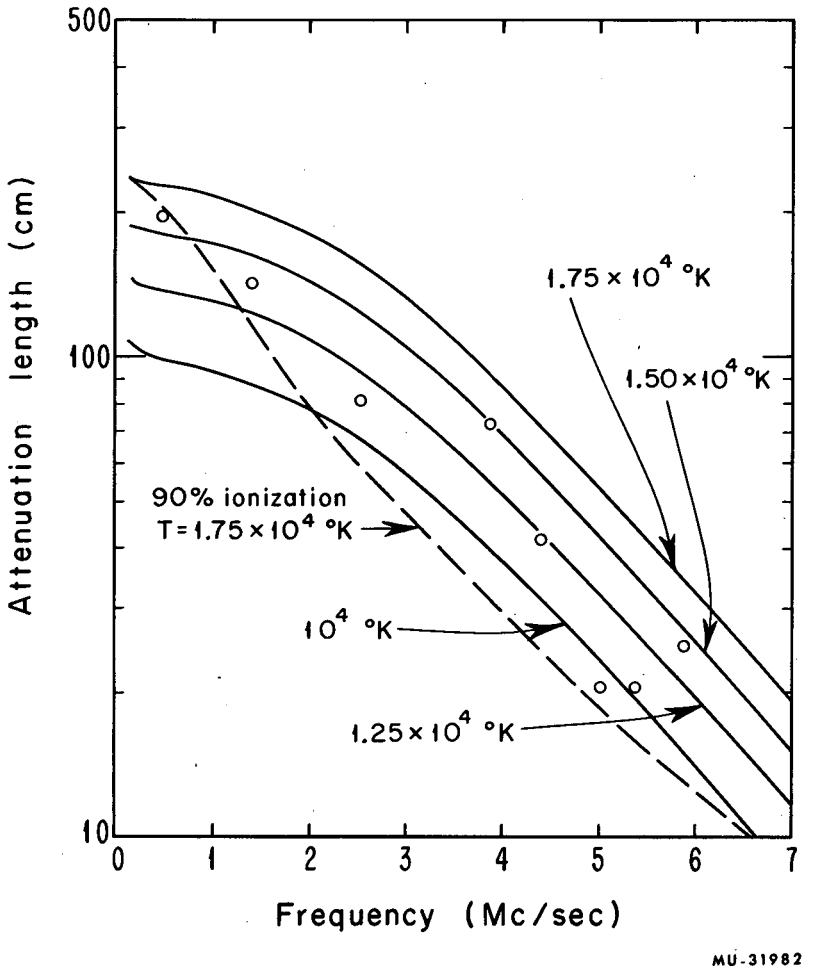

Fig. 32. Attenuation length versus frequency. The circles are experimental points as determined by the slopes of lines fitted to the amplitude versus axial-position data (see Figs. 30 and 31). Theoretical curves are shown for the first Bessel mode and a plasma radius of 7 cm. Solid curves are for 100% ionization, the spectroscopically measured average ion density ($2.85\times10^{15}/cm^3$), and four temperatures. The dashed curve is for 90% ionization, a total (ions + atoms) particle density of $2.85\times10^{15}/cm^3$ and a temperature of 1.75×10^4°K. We assume a charge-exchange cross section of 5.7×10^{-15} cm^2.

C. Mixing of Wave Types

In Section II-D we have shown theoretically that a substantial amount of the magnetic field at the driving end goes into excitation of the compressional mode at the higher frequencies. Furthermore the attenuation length for the compressional mode is larger than that for the torsional mode at high frequencies. One may therefore expect that at some sufficiently high frequency the compressional mode will dominate. This is experimentally obvious from the excitation and observation of waves above ion-cyclotron frequency, where the torsional mode should be damped out in very short distances (see Fig. 2).

In order to study the transition from propagation of the torsional mode to propagation of the compressional mode, the phase of b_θ relative to b_r was measured over the frequency range 0.485 Mc/sec to 14.5 Mc/sec (0.04 to 1.2 times ion-cyclotron frequency) at a distance of 31.4 cm from the driving end plate. The experimental results, together with the theoretical curves for the T wave and the TLA wave are shown in Fig. 33.

Each point in Fig. 33 is an average over data from 15 shots. The relative phase angle at 0.485 Mc/sec is probably small simply because of difficulties in measuring due to small b_r/b_θ. At frequencies below 4 Mc/sec, a number of large deviations from the average occurred, several differing from the average by more than 90 deg. The tendency of these large deviations was to lower the average.

The centers of the two coils used to measure b_θ and b_r are separated along the probe by 0.66 cm. A phase shift appears in the measurements, due to the finite wave transit time between the coils. To allow a correction for this phase shift, the probe was rotated 90 deg so that b_r and b_θ coils were interchanged, and more data were taken at selected frequencies. These points are also shown in Fig. 33. From Fig. 33 we see that the relative phase changes sign between 5.03 and 5.37 Mc/sec. We shall refer to the frequency at which the phase changes sign as the transition frequency.

Transition data were obtained on four different occasions. Figure 33 shows data taken with the probe most carefully aligned. The transition was usually more gradual than that shown in Fig. 33, the

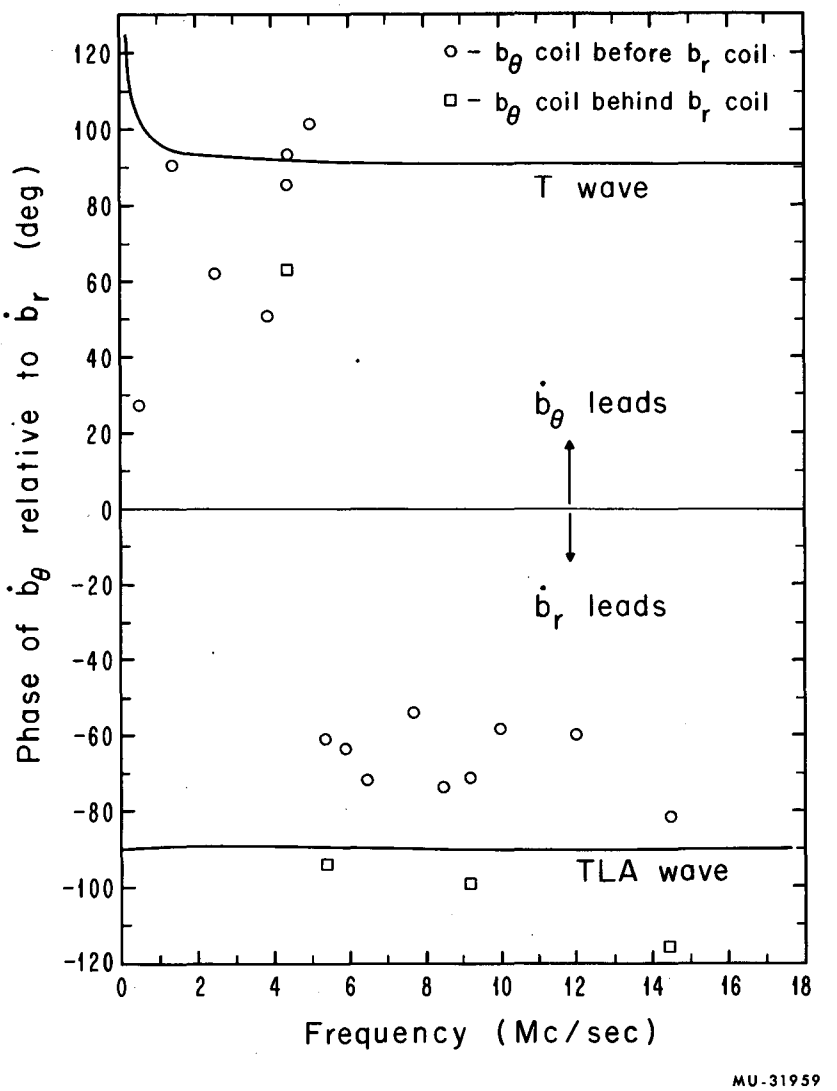

Fig. 33. Phase of $\dot{b}_\theta$ relative to $\dot{b}_r$ at 31.4 cm from the driving-end plate. Each point is an average of data from 15 shots. The points have not been corrected for finite coil spacing. Data are shown for the b_θ coil in front of the b_r coil (circles) and for the b_r coil in front of the b_θ coil (squares). Theoretical curves are shown for the two wave types at a temperature of 1.25×10^4 °K, for an ion density of $2.85 \times 10^{15}/cm^3$ (the measured average density), no neutral particles, the first Bessel mode, and a plasma radius of 7 cm.

steepness of the transition being slightly different each time. However, the transition frequency was between 5.03 and 5.37 Mc/sec in every instance. (One may note in Fig. 6 that the theoretical A_{12}/A_{11} at the driving end drops sharply to 1 at about 5.1 Mc/sec.)

Similar data for two gas pressures and a distance of 7.6 cm from the driving end plate are shown in Fig. 34. Comparing data on this figure with the previous figure is somewhat difficult because a probe so close to the driving end has been found to perturb the plasma (see next section). We do note, however, that the transition frequency increased at the lower gas pressure. This is as expected, because at the lower pressure the TLA cutoff frequency increases, as do the excitation resonance frequencies that occur at $\lambda_{ni} = 2\pi a$ (see Sec. II-D).

The ratio of the components $\dot{b}_r/\dot{b}_\theta$ has been measured from the same data used for Fig. 33 and is shown with the theoretical curves for the two wave types in Fig. 35.

The phase measurements of the preceding paragraphs do not present the complete picture of the transition from torsional to compressional mode. As may be seen from the theoretical curves of Fig. 35, at 6 Mc/sec for the TLA (compressional) wave, we have $b_\theta = 0.7\, b_r$, and for the T(torsional) wave, $b_r = 0.7\, b_\theta$. One therefore expects to observe the TLA wave in the b_r signal at a lower frequency than in the b_θ signal. This expectation is realized by examination of the $\dot{b}_\theta$, $\dot{b}_r$ oscilloscope traces for frequencies near the transition frequency. From Fig. 36 we see that the compressional wave enters the $\dot{b}_r$ signal at about 5 Mc/sec. At 5.9 Mc/sec it also causes significant perturbation in the $\dot{b}_\theta$ signal. At higher frequencies the compressional wave dominates entirely.

Because of the appearance of the compressional mode, the amplitude measurements at 5.87 Mc/sec may be somewhat questionable. It is expected that the time-of-arrival measurements are still correct, because even at 60.3 cm the $\dot{b}_\theta$ signal is still predominantly due to the torsional wave, and one can still identify the appropriate peak for the time-of-arrival measurement.

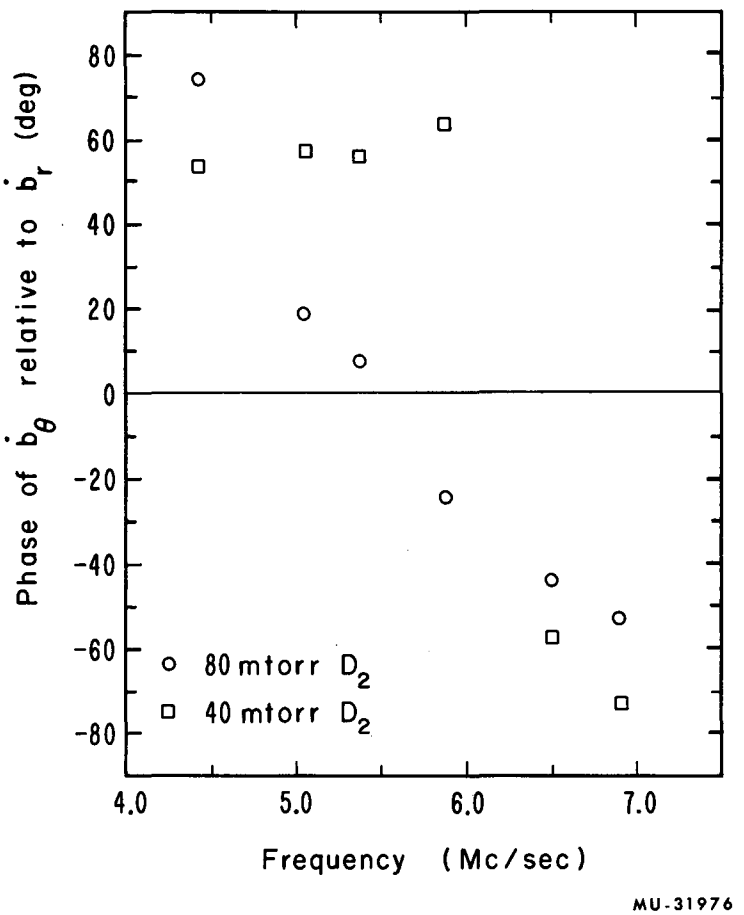

Fig. 34. Phase of $\dot{b}_\theta$ relative to $\dot{b}_r$ for two gas pressures at 7.6 cm from the driving-end plate.

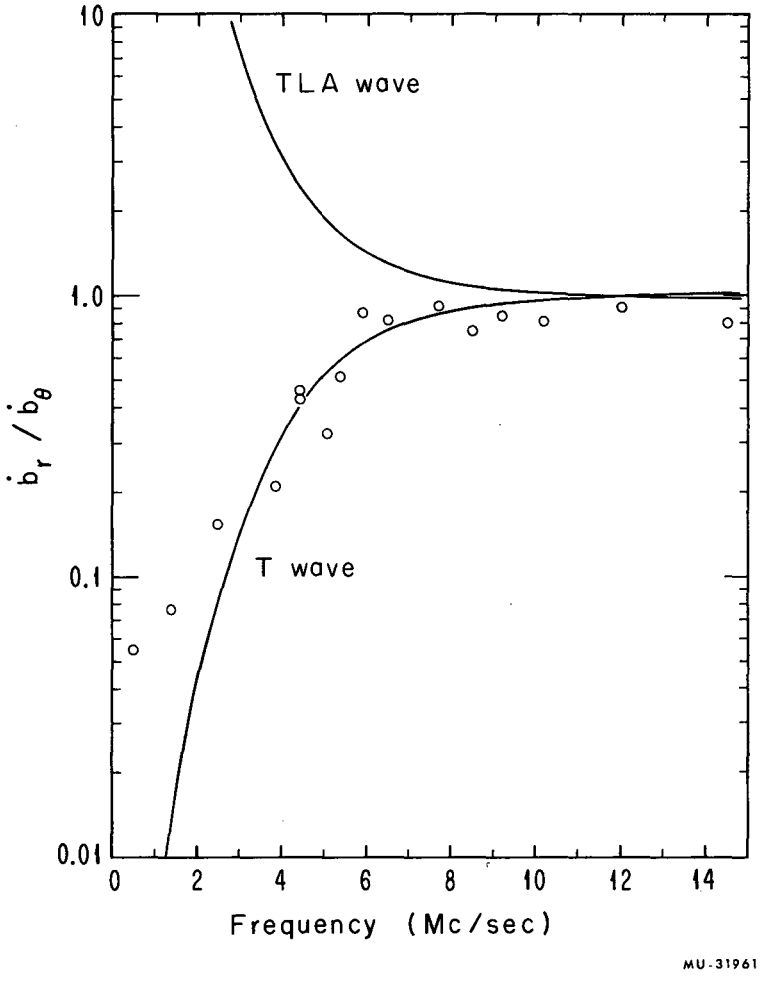

Fig. 35. Frequency versus $\dot{b}_r/\dot{b}_\theta$ from the same data as Fig. 33. Theoretical curves are shown for the two waves (calculated for the same parameters as those in Fig. 33).

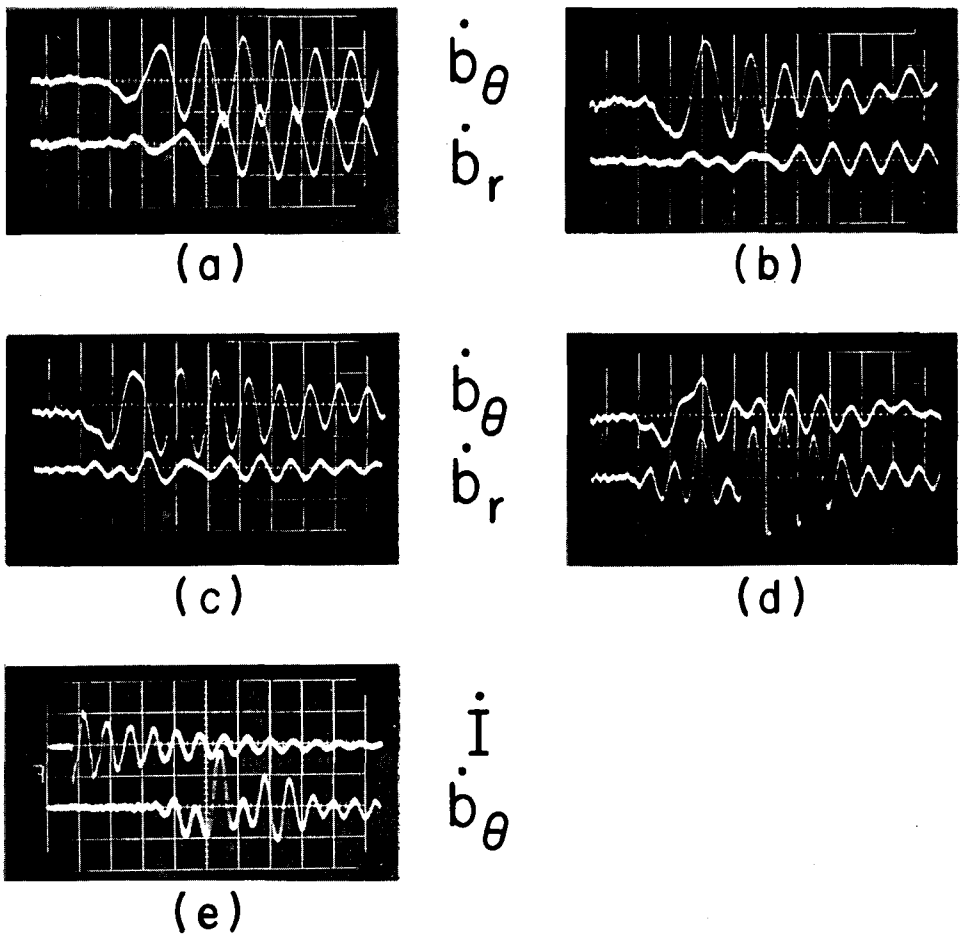

Fig. 36. Traces of $\dot{b}_\theta$ and $\dot{b}_r$ showing mixture of wave types. The sweep speed is 0.2μsec per large division for all cases. The axial position is 60.3 cm from the driving end for (a) through (d). For (e) the axial position is 43.2 cm. We note for the various traces: (a) 4.41 Mc/sec. Here $\dot{b}_\theta$ and $\dot{b}_r$ are relatively undistorted. The early $\dot{b}_\theta$ signal may be observed to be of lower frequency than the rest of the wave train, and correspondingly the early part of $\dot{b}_r$ is of low amplitude. (b) 5.03 Mc/sec. The $\dot{b}_\theta$ signal does not differ significantly from that at 4.41 Mc/sec; however, we see a hint of interference between the wave types in the early part of $\dot{b}_r$. We may also observe a reflected wave at 1.8 μsec. (c) 5.37Mc/sec. The compressional wave is now more obvious in the early part of the $\dot{b}_r$ signal, and an interference between the two wave types may be seen at about 0.8 μsec. (d) 5.87 Mc/sec. There is now also a noticeable mixing of wave types in the $\dot{b}_\theta$ signal. An apparent interference between wave types may again be seen at about 0.8 μsec. A reflection, may be observed at 1.7 μsec. (e) 6.9 Mc/sec. Here $\dot{b}_r$ is not shown, but rather the derivative of the wave current and $\dot{b}_\theta$. On the $\dot{b}_\theta$ trace one sees the compressional wave, with the low-frequency early part of the torsional mode superimposed. The small distortions apparent in the current trace are caused by ringing in the cables that connect the ionizing-current bank to the electrodes.

D. Perturbation of the Plasma by Probe Tubes

On some shots on which the velocity and attenuation were measured the wave signal was also monitored by another probe at the same radius as the moving probe but at a fixed distance of 66 cm from the driving end. Time of arrival at the stationary probe vs axial position of the moving probe is shown for two frequencies in Fig. 37. From this figure we see that the time of arrival is not greatly affected by the presence of the probe tube in the plasma, and hence we expect that the plasma density is not affected much by the presence of the probe.

A plot of wave amplitude at the stationary probe vs axial position of the moving probe is shown in Fig. 38. This figure seems to indicate that there is not significant perturbation for a probe position of 43.2 cm, but there is significant perturbation for axial probe positions of 31.4 cm and less.

This does not necessarily imply that the plasma between the driving end and the end of the probe tube is affected. For an axial position of 31.4 cm, no changes are observed in the propagation of the ionizing front, and the wave amplitude as measured there fits an exponential curve as well as the points for other axial positions. For an axial position of 20.3 cm, however, the average velocity of the ionizing front decreases by about 10%. Furthermore, the measured average wave amplitude at 20.3 cm is smaller than for larger distances from the driving end. In view of the considerations of this section, 31.4 cm is the shortest distance from the driving-end plate for which amplitude measurements were used in calculating attenuation lengths.

E. Discussion of Errors

Standard deviations for time of arrival measurements are quite small and therefore are not discussed here. Unfortunately, the amplitudes were much less reproducible. Their scatter is perhaps due primarily to temperature fluctuations and azimuthal asymmetry.

For a wave time and crowbar time which gave greater amplitude scatter than that reported in the previous section, the data were examined for evidence of azimuthal asymmetry. Two probes 180 deg apart, both at a radius of 3.55 cm and an axial position of 66.0 cm, were used

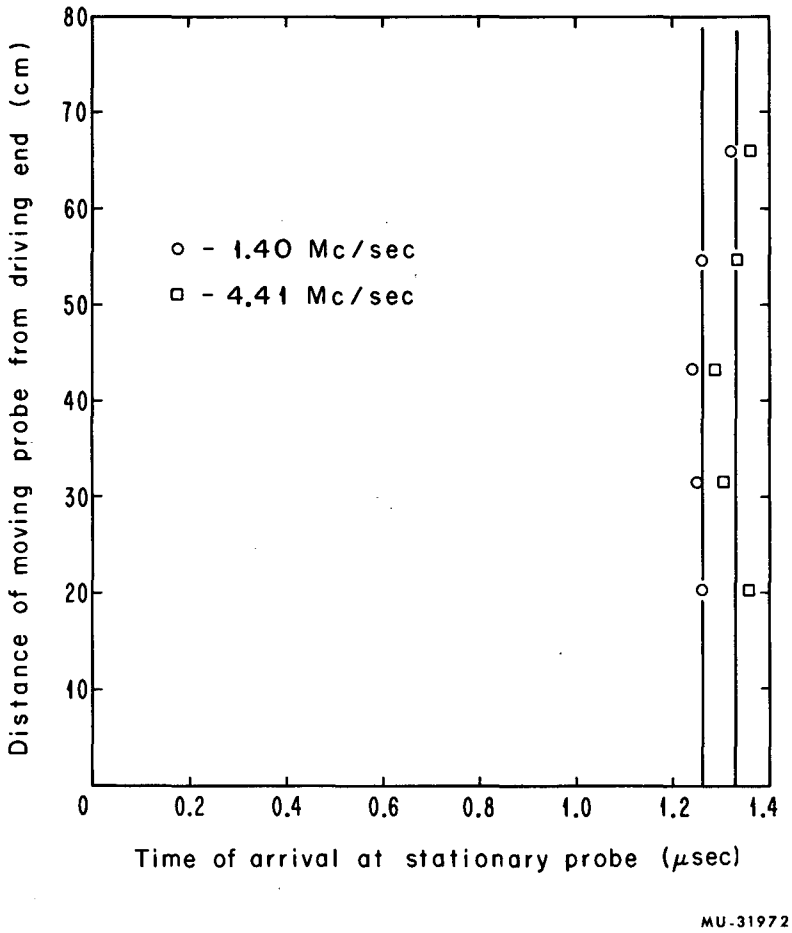

Fig. 37. Time of arrival at a probe near the receiving end (66 cm from driving-end plate) versus position of another probe tube.

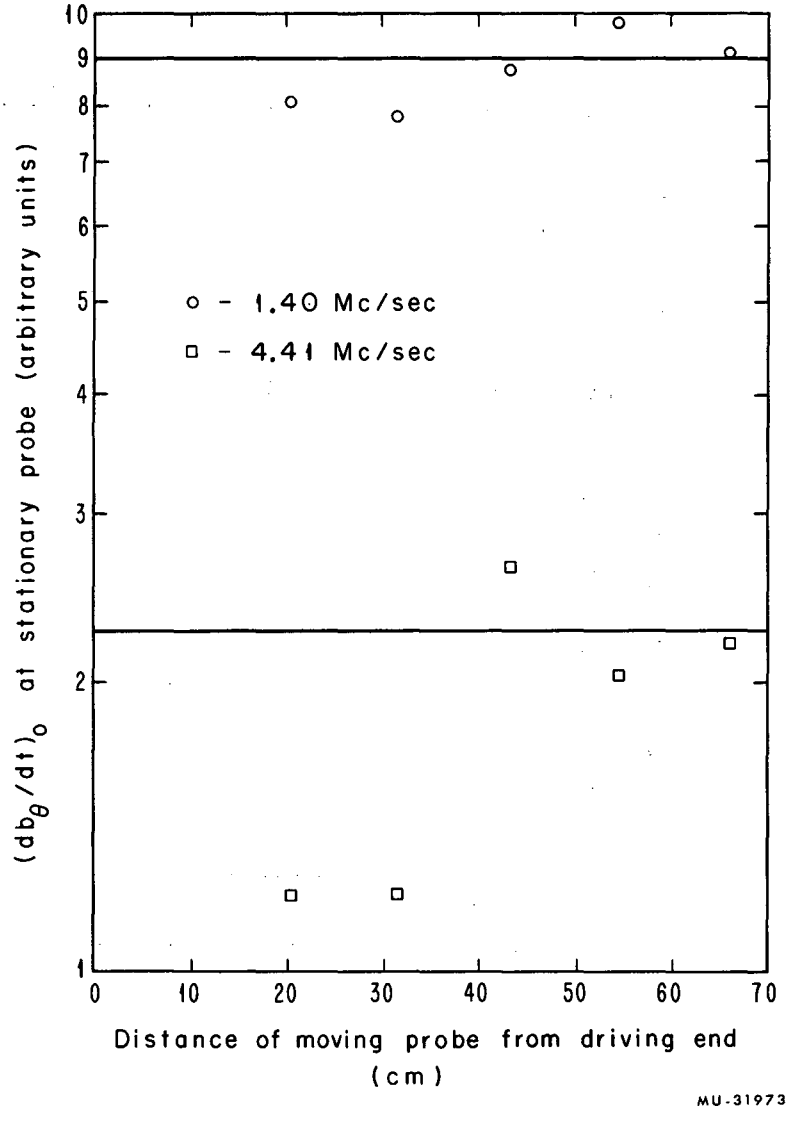

Fig. 38. Wave amplitude as observed by a probe 66 cm from the driving-end plate versus position of another probe tube.

to observe a 4.41-Mc/sec wave. If the fluctuations were due primarily to asymmetry, one would expect the sum of the amplitudes measured by the two probes to have smaller scatter than would be calculated on the basis of independent signals. If instead, the scatter were due to a shot-to-shot temperature variations of the entire plasma, the reverse condition would be expected. For data taken from 21 shots, the standard deviation of the sum of the two amplitudes differed by only 8% from that expected on the basis of independent measurements with the two probes. (i.e., the scatter behaves as if each probe were in its own plasma, completely independent of the other). This suggests that temperature and asymmetry effects are equally important.

No correlation was observed between deviations in time of arrival and deviations in amplitude.

In order to ascertain if any asymmetries originated in the wave drive, the electrode Rogowski belt was replaced by a four-coil magnetic probe. The probe was held in place midway between the center electrode and the wall by a polystyrene form which could be rotated about the electrode axis. The ionizing-current and wave-current signals were observed for a number of shots, and the polystyrene form (with probe) was twice rotated 90 deg and the measurements repeated. The measurements were made at 4.4 Mc/sec.

For a fixed probe position, the amplitude had an average deviation of 4% from the average amplitude. The corresponding average deviation from Rogowski-belt measurements was 2%. No significant distortions were seen in the wave form. The average amplitude observed after rotating the probe about the electrode (new azimuthal position) agreed with the average as measured at the initial position.

From the above we may conclude that if there is an asymmetry in the wave drive, it starts from a random spot on the electrode. If we assume that the asymmetry is in the nature of a current spoke that leaves the tip of the electrode and flows in a diametrical plane to the wall, on the average this spoke represents about 2.5% of the total wave current.

We note in passing that the probe did observe a rotating spoke in the ionizing-current signal. A spike on the current trace initially

rose about 30% above the rest of the current signal. Observations at the various azimuthal positions indicated a spoke rotation in the $\underset{\sim}{E} \times \underset{\sim}{B}$ direction with a 3.8-μsec period. A spoke also appeared as a filament of light in Kerr-cell photographs of the breakdown.

As noted in Sec. III-B-3, the standard deviation for a set of nine temperature measurements at a radius of 3.35 cm was 4%. This implies a 12% probable error for a single shot. At 5 Mc/sec and for an axial position of 64 cm and a temperature of 1.25×10^4 °K, such a temperature change of the plasma as a whole would change the wave amplitude a factor of 2. The observed temperature variations are then larger than necessary to produce the observed amplitude variation. Temperature measurements, however, are made using a collimated beam of light from the plasma, and asymmetries may contribute to the observed scatter. The waves, on the other hand, may tend to effectively average over such asymmetries to some degree.

As mentioned before a more serious problem with the attenuation measurements was that on most plots of the amplitude vs axial position, one point fell far off an exponential curve. The reason is not known.

Scatter in the measurements of the relative phase between b_r and b_θ was a serious problem at frequencies below 4.4 Mc/sec. Plasma asymmetries are probably partly to blame, but there is also the possibility of contributions to the signal from currents flowing along the probe tubes or local plasma perturbation by the probe tubes. There were sometimes deviations of greater than 90 deg from the average for frequencies below 4.4 Mc/sec.

V. CONCLUSIONS

We have measured the phase velocity of the torsional hydromagnetic wave for frequencies from 0.04 to 0.48 times ion-cyclotron frequency and found general agreement, within experimental errors, with the theoretical prediction for a uniform plasma having an ion density equal to the spectroscopically measured average ion density. Measurements of wave attenuation were less successful than velocity measurements; however, within the uncertainties of the experiment, the results agreed with theory.

The high-frequency limit to the velocity and attenuation measurements was due to entry and domination of the compressional wave. Above 4 Mc/sec, the attenuation of the compressional wave is low, and at higher frequencies the coaxial-electrode wave-generating system excites this type of wave appreciably.

Many of the difficulties encountered in this experiment are probably due to the lack of a uniform plasma. Better reproducibility has been obtained in noble-gas plasmas (see Jephcott and Stocker[12]) but no method are generally known for making completely ionized uniform deuterium (or hydrogen) plasma. Another possible difficulty associated with this plasma production technique is that radial probe tubes appear to cause serious plasma perturbations. A nonrotating plasma would not be as largely affected by radial probes, and radial probes could be made small more easily than long axial probes.

For further studies of the propagation of the torsional mode, a better ionization mechanism is desirable. Lower ion density and perhaps a smaller hydromagnetic-wave-guide diameter is also desirable, so as to push the entry of the compressional wave to higher frequencies. There is also a possibility of designing a driving system that provides the proper ratios and phases of r, θ, and z field components to selectively excite one or the other of the two wave types.

A brief unsuccessful attempt was made in this experiment to extend the measurement range in frequency by placing a set of closely spaced conducting rings close to the plasma at the driving end, thereby increasing the torsional-wave-excitation resonance frequency of Eq. (2.29).

The lack of success may be an indication of inadequacy of the theory of wave excitation of Sec. II-D. In combination with the apparently different wave behavior near the electrode as observed in the velocity measurements, it indicates that the approximation of negligible electrode length may not be good.

The dispersion of the torsional wave has been measured in ionized air by Nagao and Sato.[11] Comparison with their work is difficult, however, since different ionic species are present in the plasma, and their plasma properties are not known. Jephcott and Stocker[12] recently performed dispersion measurements in neon and argon plasmas. They obtained results that agree well with theory but are not readily comparable with results of this experiment because of the difference in methods. They varied the static magnetic field instead of the frequency, which changes the Alfvén velocity as well as the ratio of wave frequency to ion-cyclotron frequency.

APPENDICES

A. The Assumption of Axial Propagation

In Section II-B we stated that we would assume purely axial propagation, which would imply restrictions on the k_c. By purely axial propagation we mean that there are no time-dependent distortions on the radial profile, i.e., there exist radial modes in the tube which may be propagated down the tube with a change in amplitude but no change in radial distribution. We now show the necessity for the restrictions on k_c.

We first note that we may write

$$f(r)e^{-\omega t}$$

in the form

$$|f(r)| \exp\left\{i\left(\tan^{-1}\frac{\text{Im } f(r)}{\text{Re } f(r)} - \omega t\right)\right\}, \tag{A-1}$$

which has a time-dependent distortion unless $[\text{Im } f(r)]/[\text{Re } f(r)]$ is a constant, or Re f(r) is zero. In particular, the case $|f(r)| = \text{const}$, and $\tan^{-1}[\text{Im } f(r)/\text{Re } f(r)]$ proportional to r signifies a radially propagating wave.

We return to Eq. (2.16) and require

$$\frac{\text{Im } b_\theta(r)}{\text{Re } b_\theta(r)} = \text{constant} \equiv E. \tag{A-2}$$

[The case Re f(r) = 0 may be treated similarly with the same conclusions we reach here.] We use the power-series representation of the Bessel function,

$$J_n(z) = \sum_{m=0}^{\infty} \frac{(4)^m (z/2)^{n+2m}}{m!(n+m)!} . \tag{A-3}$$

Since we require condition (A-2) for all r, it must hold independently for each power of r in the series expansion. Therefore we obtain from Eqs. (2.16), (A-2), and (A-3)

$$\mathrm{Im}\left[C_1({}_1k_c)^{2m+1} + C_2({}_2k_c)^{2m+1}\right] = E\left\{\mathrm{Re}\left[C_1({}_1k_c)^{2m+1} + C_2({}_2k_c)^{2m+1}\right]\right\}, \tag{A-4}$$

which must hold for all nonnegative integral values of m.

Equation (A-4) implies a relationship between the real and imaginary parts of the two k_c. We may write Eq. (2.15a) in the form

$$({}_1^2k_c)^2 = a + ib \pm (c + id), \tag{A-5}$$

and we may see that for example, the special case $E = \mathrm{Im}\, C_{\frac{1}{2}} = \mathrm{Im}({}_{\frac{1}{2}}k_c)^2 = 0$ requires $b = d = 0$. This is a set of two equations in the three variables Im p, Re p, and ω, and comprises a dispersion relation that is independent of k_c, hence independent of geometry. Other relations between real and imaginary parts of the k_c which would arise as solutions to Eq. (A-4) when substituted into Eq. (A-5) may be expected to give geometry-independent dispersion relations also. We reject geometry independence as unphysical, and therefore set $C_2 = 0$ in Eq. (2.16) and restrict our solution to

$$b_\theta = C_1 J_1(k_c r). \tag{2.17}$$

The procedure we have used here to eliminate one Bessel function is justified only if one term in Eq. (2.16) is sufficient to satisfy boundary conditions. For a general set of boundary conditions, one must allow the possibility of radial variations in time. In Appendix B, we investigate a particular case in which radial propagation is observed.

B. A Plasma Surface Wave

A radial wave propagation has been observed during the course of this study. An investigation of the phenomena was carried out under experimental conditions similar to those reported in Section III except a hydrogen plasma was used instead of a deuterium plasma and a fixed frequency of 3.1 Mc/sec was used.

The radial propagation was first noticed as an apparently anomalous behavior for waves excited after the plasma had decayed an appreciable amount. While studying the behavior of Alfvén waves induced at various times in the decaying plasma, a sudden increase in the apparent velocity was observed for a wave time of about 220 μsec. Closer examination of the wave form at a fixed radial and axial position and various wave times revealed a small peak appearing before the Alfvén wave (see Fig. 39a) which grew in amplitude for later wave times (Fig. 39, b through d). Studies of the time of arrival and amplitude of this "precursor" peak at different axial and radial positions and various wave times led to the conclusion that it was due to a wave traveling at high velocity along the field lines near the wall (surface wave) and propagating (or diffusing) radially into the plasma. Presumably this wave involves currents in the copper wall.

Time of arrival and amplitude of both surface wave and Alfvén wave were measured as a function of radius by placing a probe in a curved probe tube, which by rotation could vary the radial position of the probe coil from near the wall to 2.25 cm from the center of the tube. Measurements as a function of axial position used a straight probe tube. The time of arrival of the surface wave vs radius is shown for a wave time of 210 μsec in Fig. 40.

Peak amplitudes of the surface wave and Alfvén wave vs frequency are shown in Fig. 41 for a wave time of 180 μsec. For later wave times the width of the Alfvén-wave profile decreases and the width of the surface-wave profile increases, i.e., the surface wave penetrates deeper toward the center of the tube.

The times of arrival of Alfvén-wave and surface-wave vs axial position for a fixed radius are shown in Fig. 42. The slope of the line drawn through the surface-wave points should not be interpreted literally as an axial velocity, because the radial velocity may be dependent on axial position.

Figure 43 shows the surface-wave amplitude vs axial position for a fixed radius. The nature of this wave can be described by the following analysis. In our analysis in the main text we assumed the wave

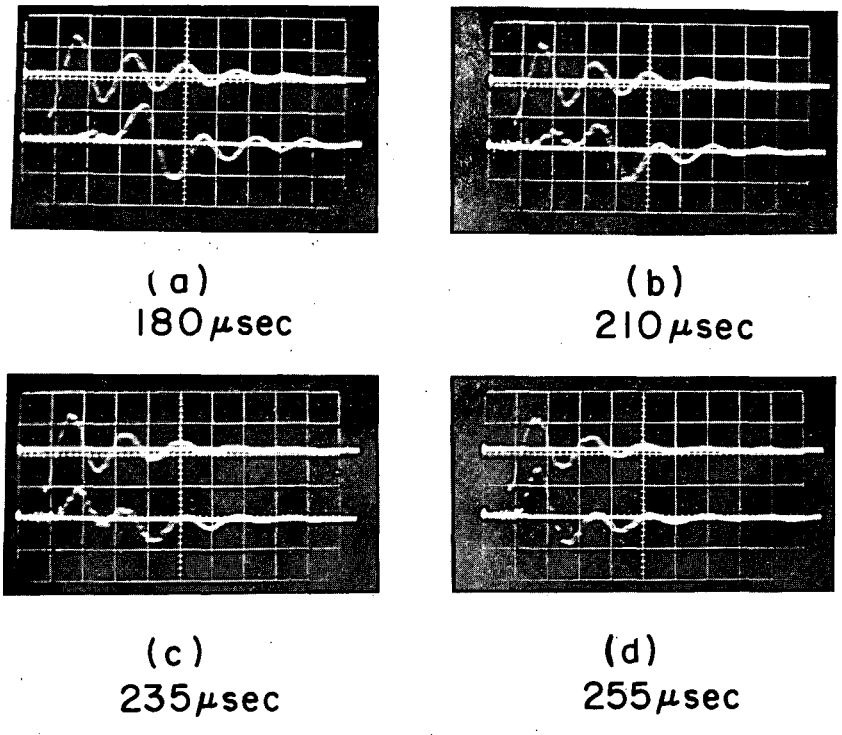

Fig. 39. Appearance of surface wave on probe signals. Wave times are given beside pictures. Top trace is dI/dt of wave exciter; bottom trace is db_θ/dt at probe. On shot (a) the surface wave is barely visible. By 255 μsec, shot (d), the surface wave dominates. Gains are the same for all four shots. The probe is at midplane and 4-cm radius.

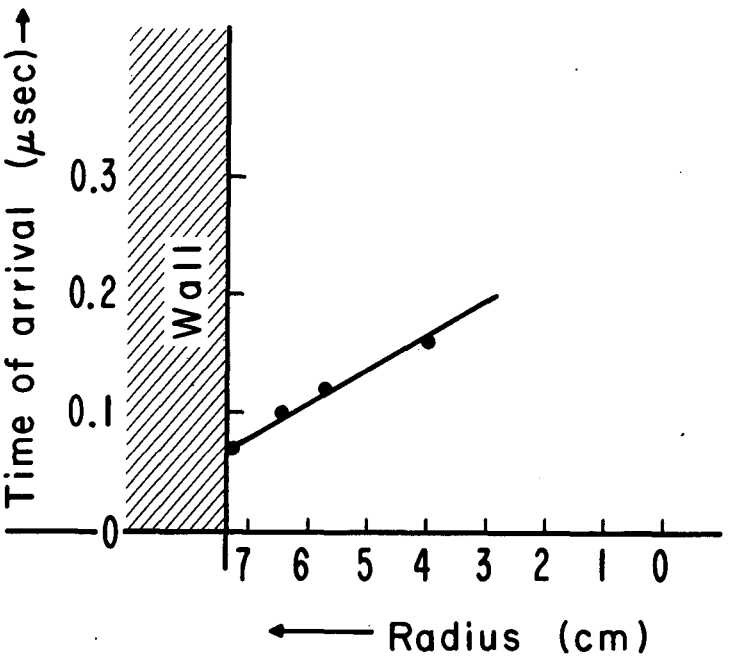

Fig. 40. Time of arrival of surface wave versus radius at midplane. The wave time is 210 μsec. Each point is an average of three shots.

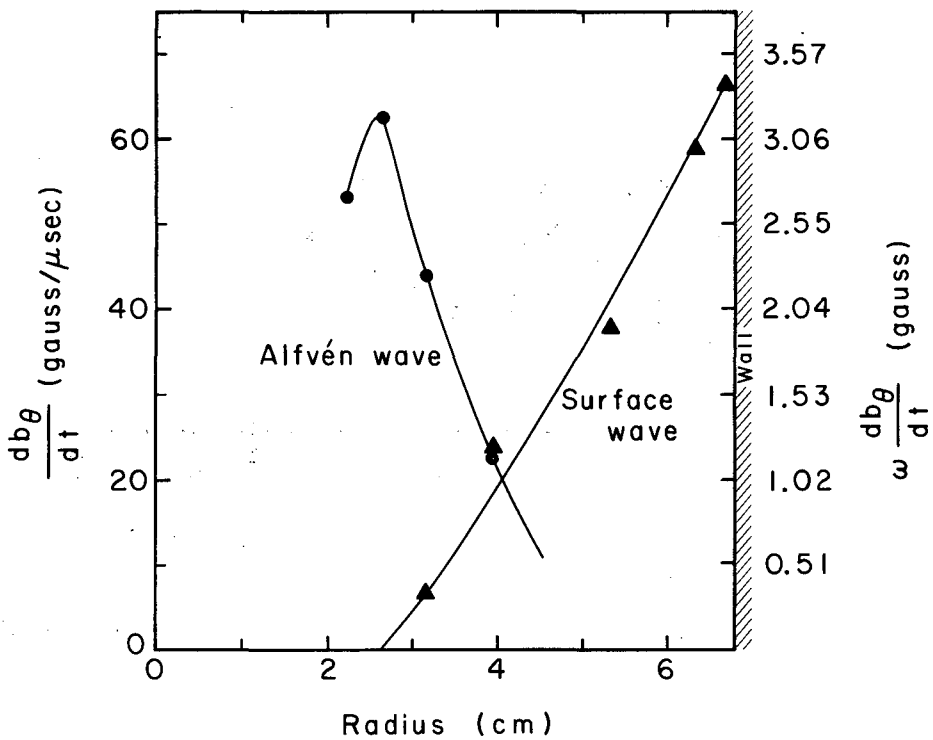

Fig. 41. Alfvén-wave and surface-wave amplitudes as a function of radius at midplane. The wave time is 180 μsec. Each point is averaged over three shots.

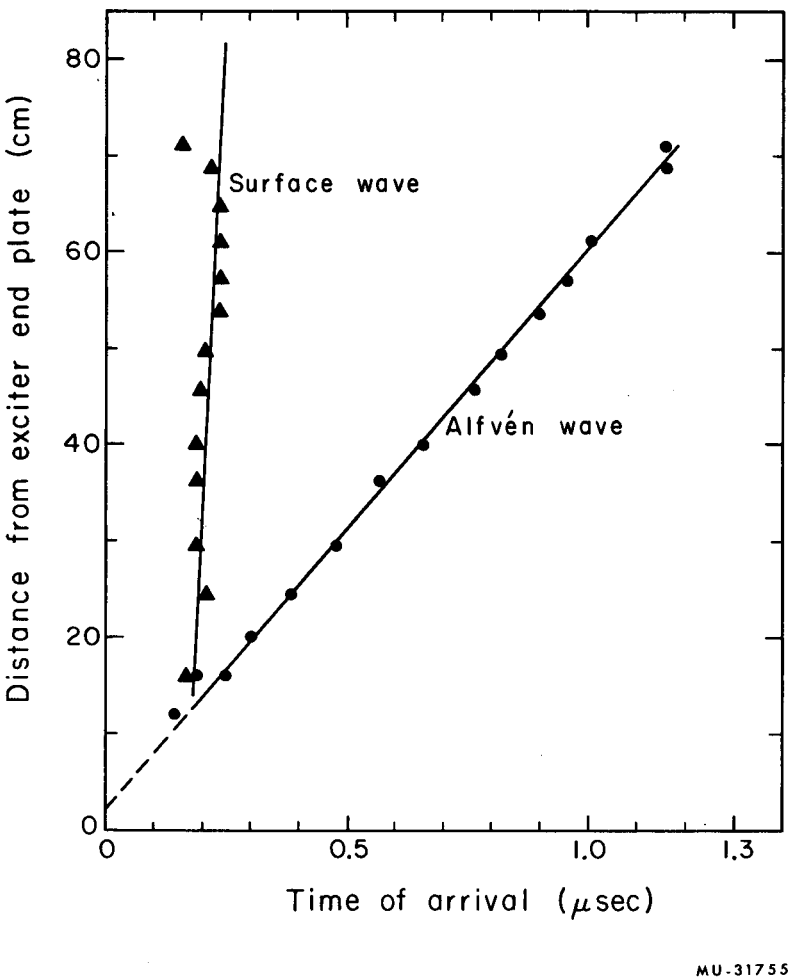

Fig. 42. Times of arrival of surface and Alfvén waves as a function of axial position. The radius is 4.8 cm and the wave time 132 μsec. Each point is an average over three shots. Below the intersection of the two lines, the Alfvén and surface waves are not readily distinguishable.

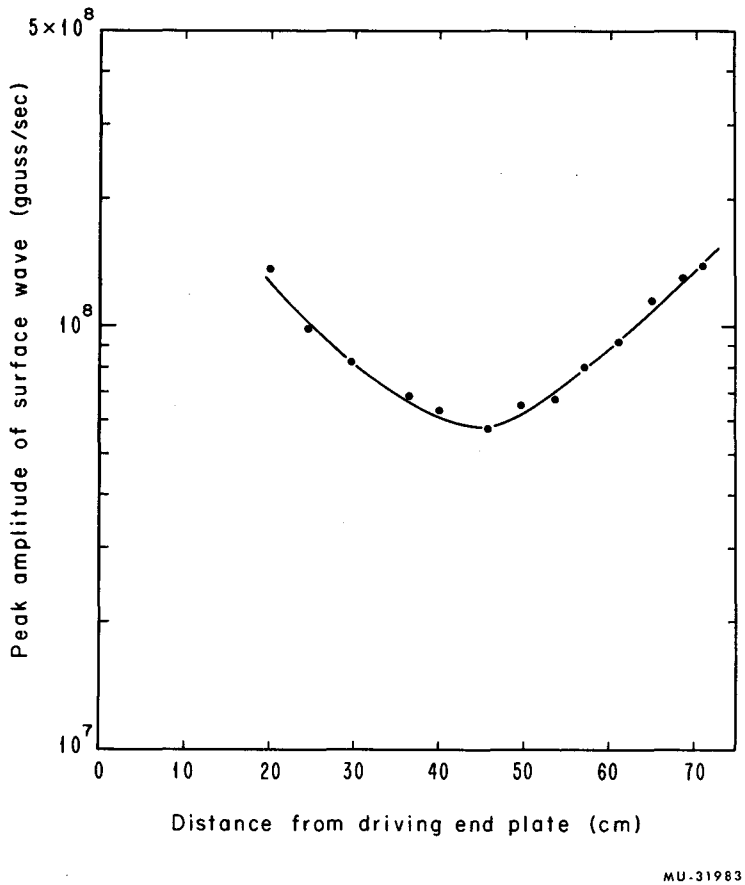

Fig. 43. Surface-wave amplitude versus axial position at a radius of 4.8 cm and a wave time of 225 μsec. For distances of less than 20 cm from the driving-end plate, the surface and Alfvén wave are not sufficiently separated to allow an amplitude measurement on the surface wave.

to be propagating in the direction of the axial static magnetic field only. We now consider the possibility of radial propagation in a special case. For the sake of simplicity we use the quasi-static equations and a Cartesian coordinate system. We replace θ by y and r by x, denote vectors parallel and perpendicular to the magnetic field by $\parallel$ and $\perp$, respectively, and assume all wave quantities are harmonic, such that $\partial/\partial t = - i\omega$. Initially we assume

$$\underset{\sim}{b} = \hat{y} b(x) e^{ipz} .$$

The basic equations in quasi-static form are

$$\frac{\partial (n_i m_i \underset{\sim}{v}_i)}{\partial t} = \underset{\sim}{j} \times \underset{\sim}{B}_0 ; \qquad \nabla \times \underset{\sim}{E} = - \frac{\partial \underset{\sim}{b}}{\partial t}$$

$$\underset{\sim}{E}_{\parallel} = \eta \underset{\sim}{j}_{\parallel} ; \qquad \underset{\sim}{E}_{\perp} = - \underset{\sim}{v}_i \times \underset{\sim}{B}_0 ; \text{ and } \nabla \times \underset{\sim}{b} = \mu_0 \underset{\sim}{j} ,$$

where we have neglected the resistive contributions to the perpendicular electric field. From the basic set we may easily obtain the wave equation

$$i \left(\omega - \frac{p^2 B_0^2}{m_i n_i \omega \mu_0} \right) b = \frac{\eta}{\mu_0} \frac{\partial^2 b}{\partial x^2} . \qquad \text{(B-1)}$$

We assume a solution of the form

$$b(x) = G_1 e^{-i\Gamma x} + G_2 e^{i\Gamma x} . \qquad \text{(B-2)}$$

The usual procedure is to solve for the axial propagation constant p in terms of Γ and the other parameters. We will instead solve for Γ, obtaining

$$\Gamma = \left(i - 1 \right) \left(\frac{\mu_0 \omega}{2 \eta} \right)^{1/2} \left[1 - \left(V_A \right)^2 \left(\frac{p}{\omega} \right)^2 \right]^{1/2} ,$$

where the Alfvén-wave speed is

$$V_A \equiv \frac{B_0}{(n_i m_i \mu_0)^{1/2}} .$$

The propagation speed along field lines, $\omega/\mathrm{Re}\ p = v_z$, is usually considered to be approximately the Alfven speed, V_A. However, if we allow the assumption of $v_z >> V_A$, then the imaginary part of p/ω is not important and we may write

$$\Gamma = \left(i - 1\right)\left(\frac{\mu_0 \omega}{2\eta}\right)^{1/2} \left[1 - \left(\frac{V_A}{v_z}\right)^2\right]^{1/2} \approx \left(i - 1\right)\left(\frac{\mu_0 \omega}{2\eta}\right)^{1/2} . \qquad \text{(B-3)}$$

Thus we see that the assumption of a propagation along field lines at much greater speed than Alfvén speed leads to the familiar skin-depth equation. We assume that the plasma occupies the region of space $x > 0$, and Eq. (B-2) reduces to

$$b(x) = Ge^{i\Gamma x} . \qquad \text{(B-2a)}$$

This signifies a wave that propagates in the x direction with velocity

$$v_x = \left(\frac{2\omega\eta}{\mu_0}\right)^{1/2}$$

and has an attenuation constant

$$\gamma \equiv \mathrm{Im}\ \Gamma = \left(\frac{\omega\mu_0}{2\eta}\right)^{1/2} .$$

The measured radial velocity is about 30 cm/μsec for wave times from 150 to 240 μsec, which indicates a temperature of about 0.24×10^4 °K in the region of propagation of the surface wave.

The surface-wave amplitudes are not exponential with radius. Particularly, late in time the radial amplitude profile is flat at the wall and steepens at smaller radii. This is probably due to cylindrical geometry and radial nonuniformity of temperature. Rough estimates for γ were

obtained by assuming γ to be the reciprocal of the distance in which the amplitude falls by 1/e as measured near the half-maximum amplitude point. The average value of γ thus obtained for wave times of 100 to 240 μsec is

$$\gamma_{exp} = 0.56/cm.$$

During that interval of wave time, fluctuations in v_r and γ are not systematic with wave time.

The value of γ corresponding to $v_r = 30$ cm/μsec is 0.67/cm.

In Fig. 43 we see that the amplitude has a minimum near midplane. This suggests a strong axial temperature inhomogeneity in the annular region from 4.8 cm radius to the wall with the temperature highest at midplane.

All the experimental results discussed above were taken with a screen in the end of the tube. The surface wave have been observed when the screen was not present but has not been studied in detail.

The temperature in the region of propagation of the surface waves has not been measured independently. The techniques reported in Section III do not work when the temperature drops below about 10^4°K, because of large continuum contributions from the H^- spectrum.

ACKNOWLEDGMENTS

The author wishes to thank Drs. Wulf B. Kunkel, John M. Wilcox, Forrest I. Boley, and Mr. William R. Baker for advice and encouragement during the course of this work. The author is indebted to Dr. William S. Cooper III for advice and instruction on the spectroscopic measurements and to Mr. Dennis A. Reilly for help in taking spectroscopic data and in data reduction.

The author wishes to express his deep appreciation to Colonels Edward B. Giller, Raymond A. Gilbert, David R. Jones, and other officers of the United States Air Force whose efforts and interest made it possible for the author to complete this work.

This work was done under the auspices of the U. S. Atomic Energy Commission.

REFERENCES

1. H. Alfvén, Arkiv Mat., Astr. Fysik, 29B, 1 (1942); idem, Cosmical Electrodynamics (Clarendon Press, Oxford, 1950).
2. C. Walén, Arkiv Mat., Astr. Fysik 30A, No. 15 (1944); 31B, No. 3 (1944); 33A, No. 18 (1946).
3. E. Åström, Arkiv Fysik 2, 443 (1950); Nature 165, 1019 (1950).
4. N. Herlofson, Nature 165, 1020 (1950).
5. S. Lundquist, Phys. Rev. 76, 1805 (1949); Nature 164, 145 (1949).
6. B. Lehnert, Phys. Rev. 94, 815 (1954).
7. T. K. Allen, W. R. Baker, R. V. Pyle, and J. M. Wilcox, Phys. Rev. Letters 2, 383 (1959).
8. D. F. Jephcott, Nature 183, 1652 (1959).
9. J. M. Wilcox, F. I. Boley, and A. W. DeSilva, Phys. Fluids 3, 15 (1960).
10. Alan W. DeSilva, Experimental Study of Hydromagnetic Waves in Plasma (Ph. D. Thesis), UCRL-9601, March 17, 1961.
11. A. Nagao and T. Sato, J. Phys. Soc. Japan 15, 735 (1960); Res. Rept. Tohoku University, Sendai, Japan (1961).
12. D. F. Jephcott and P. M. Stocker, J. Fluid Mech. 13, 587 (1962).
13. D. G. Swanson and R. W. Gould, Bull. Am. Phys. Soc., Ser. II, 8, 152 (1963).
14. D. F. Jephcott, Bull. Am. Phys. Soc., Ser. II, 8, 152 (1963).
15. D. G. Swanson, An Experimental Study of Compressional Hydromagnetic Waves (Ph. D. Thesis), California Institute of Technology Technical Report No. 1, June 1963.
16. T. H. Stix, "Generalization and Thermalization of Plasma Waves," in Proceedings of the Second International Conference on the Peaceful Uses of Atomic Energy (United Nations, Geneva, 1958), Vol. 31, p. 125.
17. W. M. Hooke, F. H. Tenney, M. H. Brennan, H. M. Hill, and T. H. Stix, Phys. Fluids 4, 1131 (1961).
18. W. M. Hooke, P. Avivi, M. Brennan, M. A. Rothman, and T. Stix, Paper CN-10/165, IAEA Conference on Plasma Physics and Controlled Nuclear Fusion Research, Salzburg 1961.

19. N. I. Nazarov, A. I. Ermakov, A. S. Tobko, V. A. Bondarev, V. T. Tolok, and K. D. Sinelnikov, Paper CN-10/231, IAEA Conference on Plasma Physics and Controlled Nuclear Fusion Research, Salzburg, 1961.
20. F. I. Boley, J. M. Wilcox, A. W. DeSilva, P. R. Forman, G. W. Hamilton, and C. N. Watson-Munro, Phys. Fluids 6, 925 (1963).
21. L. Spitzer, Jr., Physics of Fully Ionized Gases (Interscience Publishers Inc., New York, 1957).
22. W. P. Allis, S. J. Buchsbaum, and A. Bers, Waves in Anistropic Plasmas (MIT Press, Cambridge, Massachusetts, 1963).
23. J. A. Stratton, Electromagnetic Theory (McGraw-Hill Book Company, Inc., New York, 1941).
24. J. M. Wilcox, W. R. Baker, F. I. Boley, W. S. Cooper III, A. W. DeSilva, and G. R. Spillman, J. Nuclear Eng., Part C, 4, 337 (1962).
25. M. H. Brennan, I. G. Brown, D. D. Millar, and C. N. Watson-Munro, Some Experimental Observations of the Characteristics of Hydromagnetic Ionizing Fronts, Wills Plasma Physics Department, School of Physics, University of Sydney, ER. 2, Dec. 1962.
26. W. S. Cooper III, An Experimental Investigation of the State of a Highly Ionized Decaying Hydrogen Plasma (Ph. D. Thesis), UCRL-10849, June 17, 1961.
27. W. B. Kunkel and R. A. Gross, "Hydromagnetic Ionizing Waves," in Plasma Dynamics, (Proceedings of the Sixth Lockheed Symposium on Magnetohydrodynamics) (Stanford University Press, Stanford, California, 1962).
28. J. M. Wilcox, W. S. Cooper III, A. W. DeSilva, G. R. Spillman, and F. I. Boley, J. Appl. Phys. 33, 2714 (1962).
29. H. R. Griem, "Plasma Spectroscopy," in Fifth Internation Conference on Ionization Phenomena in Gases, Vol. II, 1855 (Munich, 1961).
30. W. Finkelnburg and Th. Peters, "Kontinuierliche Spektren," Handbuch der Physik (Springer Verlag, Berlin, 1957), Vol. 38 (Spektroskopie II), p. 79.
31. O. A. Kerns and R. F. Tusting, "Constant Amplitude Light-Flash Generator for Gain Stabilization of Photosensitive Systems" in Proceedings of the Conference on Instrument Techniques in Nuclear

Pulse Analysis, Monterey, Calif., April 29 - May 3, 1963 (to be published); also UCRL-10895, July 18, 1963.

32. G. R. Spillman, W. S. Cooper III, and J. M. Wilcox, Appl. Optics 2, 205 (1963).

33. G. R. Spillman, G. W. Hamilton, W. S. Cooper III, and F. I. Boley, "Polychromator Modification and Data Reduction," in Controlled Thermonuclear Research Semiannual Report, UCRL-10294, July 20, 1962.